



Femtosecond laser ablation of Zn in air and ethanol: effect of fluence on the surface morphology, ablated area, ablation rate and hardness

Shazia Bashir^{1,2} · Muhammad Shahid Rafique^{2,3} · Ali Asghar Ajami^{2,4} · Chandra Sekher Nathala² · Wolfgang Husinsky² · K. Whitmore⁵

Received: 23 April 2020 / Accepted: 17 December 2020

© The Author(s), under exclusive licence to Springer-Verlag GmbH, DE part of Springer Nature 2021

Abstract

This paper reports the effect of Ti:Sapphire laser (800 nm, 30 fs) fluence on the surface morphology, ablated area, ablation rate and hardness of a femtosecond laser irradiated Zn in air and ethanol. Targets were exposed to 1000 succeeding pulses at various fluences ranging from 1.3 to 5 J cm⁻². To characterize the growth of structures on the surface of irradiated Zn, Field Emission Scanning Electron Microscopy (FESEM) has been performed. The ablation depth has been measured using a confocal microscope. Nonuniform surface morphology with an appearance of both micro and nanoscale droplets, particulates and rims has been observed in case of air-assisted ablation, whereas, in ethanol, nanoscale colloids, droplets, pores and bowl-shaped cavities have been formed. The ablation of Zn in air is responsible for deep craters with pronounced melt expulsions and ripples. Whereas, shallow and clean craters are formed in ethanol. The ablation threshold fluence is evaluated analytically and experimentally by employing three methods, i.e., squared diameter, depth ablation rate, and volume ablation rates. The hardness of irradiated targets is higher as compared to untreated Zn and shows an increasing trend with increasing fluence for both environments. However, in the case of ethanol, the hardness values are higher than air.

Keywords Femtosecond laser · Laser fluence: surface modification · Ablated area · Ablation depth · Hardness

1 Introduction

Femtosecond (fs) laser irradiation sources are highly important, popular and promising micro/nano surface structuring tools for materials modification with remarkable precision, and accuracy. The main advantages of femtosecond laser over a nanosecond pulse include; less mechanical and thermal damages in the vicinity of the processed regions, high aspect ratio along with accurate depth and volume control

[1]. In the field of laser drilling, cutting and welding, the ultrashort laser processing technology has become an indispensable choice due to its advantages of high flexibility, easy integration, automation and reproducible technique. The laser ablation process can be strongly influenced by laser beam parameters, such as wavelength, energy or fluence and pulse duration [2]. It has been also reported that the target material and ambient conditions are also very effective for the interactions [3]. The presence of ambient environment improves the ablation efficiency due to enhanced interactions of the vapor plume and background environment. There is also shock wave generation resulting in enhanced confinement of the plasma plume [4, 5].

The surface structural modification of solid materials by laser radiation involves a complex chain of processes. It includes laser energy transport, ablation mechanisms, ablation threshold, plume hydrodynamics and evolution. During fs laser ablation, the energy deposition mechanisms to the target material is broadly categorized into electronic and thermal processes and identification of these processes is complex phenomenon [6, 7].

✉ Shazia Bashir
shaziabashir@gcu.edu.pk

¹ Centre for Advanced Studies in Physics, GC University, Lahore, Pakistan

² Institute of Applied Physics, Vienna University of Technology, Vienna, Austria

³ Department of Physics, University of Engineering and Technology Lahore, Lahore, Pakistan

⁴ Faculty of Physics, Semnan University, Semnan, Iran

⁵ University Center for Transmission Electron Microscopy, Technische Universität Wien, Wien, Austria

With the use of ultrashort laser pulses non equilibrium energy distributions with large excess population in the excited states can be produced. The distinct physical processes which come into play in laser-solid interaction on the ultrafast time scale, open new routes of modifying the mechanics, structure and the morphology of materials and offer interesting perspectives in laser materials processing [8]. Direct visualization of the complete evolution of femtosecond laser-induced surface structural dynamics of metals has been reported by Fang et al. [9]. Real-time in situ study of femtosecond-laser-induced periodic structures on metals by linear and nonlinear optics has been investigated by Zhang et al. [10]. Thermodynamic pathways to melting, ablation and solidification in absorbing solids under pulsed laser irradiation are reported by Lorazo et al. [11]. Recently, using laser as a tool for micro machining, a comparative study of laser surface hardening of 50CrMo4 steel using continuous-wave laser and pulsed lasers with ms, ns, ps and fs pulse duration has been reported by Maharjan et al. [12]. The formation of nano dimensional structures on the surface of Tin(Sn) and Zirconium (Zr) exposed to femtosecond laser pulses in the ambient environment of ethanol as function of laser fluence and pulse duration has already been reported by our group [4]. In case of liquid assisted ablation the reactivity of chemical also plays vital role for the growth of surface structures [13]. The overall processes of energy coupling in case of liquid confined environment becomes significantly complex due to plume formation, bubble-cavitation, micro-jet formation and plasma shielding [14]. Researchers [15–18] have focused on the growth of the nanostructures using ethanol, water or other liquids as replacement to air because of cleaner ablation and enhanced ablation efficiency due to confinement. Thus, the nature of ambient atmosphere plays a critical role on the surface structuring of the material [4, 19, 20].

By applying various number of picosecond laser pulses at varying fluences and at the wavelength of visible (515 nm) and IR (1030 nm) region, laser ablation threshold and surface modifications of Zn have been investigated by Mustafa et al. [21–24]. The evaluation of ablation threshold is highly important for laser surface texturing of materials, pulsed laser deposition and plasma generation. The ablation threshold of solid targets has been evaluated by Chichkov et al. [25] by presenting theoretical models and quantitative analysis of experimental results. The ablation threshold of metals for ultrashort laser pulses has been reported by Nolte et al. [26]. A simple technique for measurements of pulsed Gaussian-beam spot sizes for absolute calibration of the threshold-energy fluences for pulsed laser-induced effects has been reported by Liu [27].

The purpose of the present work is to investigate the effect of variation in the irradiating fluence of a femtosecond laser on the surface morphology, ablation efficiency and

hardness of Zn in both air and ethanol environments. A Ti: Sapphire laser with central wavelength of 800 nm and pulse duration of 30 fs was employed as an irradiation source for ablation. FESEM analyses were performed to explore the surface features of the ablated Zn. The ablation threshold of Zn is evaluated analytically as well as using three experimental techniques, i.e., the squared diameter, ablation rate/penetration depth rate and volume ablation rate at various fluences first time for femtosecond pulses in both environment of air and ethanol. The variation in chemical composition and structural modifications of fs laser-ablated Zn in air and ethanol has been explored by Attenuated Total Reflectance- Fourier Transform Infra-Red (ATR-FTIR) and X-Ray Diffractometer. The mechanical behavior of irradiated targets has been analyzed by measuring micro hardness using Vickers micro hardness tester.

2 Experimental

The present experimental investigations focus on the ablation of Zn at varying fluences of a fs laser. The experiments have been performed with multiple femtosecond laser pulses in air as well as in ethanol. The grinded, polished and ultrasonically cleaned commercially available Zn specimen (with purity of 99.9%) with dimensions of 10 mm × 10 mm × 3 mm were mounted on the motorized xyz- manipulator to position the targets precisely for each exposure. The surface roughness of polished samples is 10 nm (Root Mean Square (RMS) value).

A regenerative Chirp Pulse Amplified (CPA) 800 nm Ti: Sapphire laser system (Femtopower Compact Pro, Femtolasers Produktions GmbH Vienna, Austria) with a maximum pulse energy of 1 mJ operating at 1 kHz repetition rate has been used for irradiation. It is seeded from a mode-locked Ti: sapphire oscillator (Femtosource Scientific Pro, Femtolasers Productions GmbH Vienna, Austria). The laser beam produced a Gaussian spatial distribution of energy which was monitored by a beam profiler (Laser Cam –HR Coherent). The pulse energy was measured using an energy meter (Coherent 210, USA) that was placed before the lens and the energy was varied using neutral density filters and a linear polarizer. The focused laser beam, after passing through a 20 cm focal length lens, was incident perpendicular to the surface of the target but at an out-of-focus position (2.7 mm before the focal position) giving a focused spot diameter of 100 μm ($1/e^2$ value).

In the case of ablation in the ethanol, the Zn specimen was immersed in ethanol filled in a quartz cuvette in such a way that it was lying on the bottom of the cuvette. The laser beam was brought through the uncovered top of the quartz cuvette to avoid the energy losses.

In the first part of experiment, the targets were exposed in air for pulse energies of 50, 100, 150, 200, 250, 300, 350, 400 and 450 μJ keeping the pulse duration constant at 30 fs. A half-wave plate and a polarizing beam splitter were used to control the laser pulse energy irradiating the sample surface. The corresponding fluence values are 0.6, 1.3, 1.9, 2.5, 3.2, 3.8, 4.4, 5 and 5.7 J cm^{-2} . These fluence values are the peak fluences which are related to the pulse energy E_p as

$$F = \frac{2E_p}{\pi\omega_0^2} \quad (1)$$

The second part of the experiment was carried out by exposing Zn targets under the same condition but in ethanol environment. Each exposure consisted of 1000 number of pulses for both the environments. The purpose was to explore the effect of fluence variation on laser ablation at the central as well as peripheral ablated areas of Zn. The beam path length in ethanol is 10 mm.

The surface morphology of the irradiated Zn was analyzed using a Field Emission Scanning Electron Microscope (FESEM, FEI-QUANTA 200F, Netherlands). SEM analyses were performed for both central as well as for peripheral ablated areas of Zn. The ablated areas and ablation depths of Zn for both environments at various fluence values were measured using an optical microscope (STM-6 Olympus). The crater depth was also measured with a confocal laser scanning microscope (Nano focus μsurf explorer version 7.02). For optical microscope, the resolution is 0.25 μm , For FESEM, the resolution is 1 nm and for confocal microscope, the lateral resolution is 140 nm and axial resolution is 1 μm .

To explore the variation in chemical composition and structural modifications of fs laser-ablated Zn in air and ethanol Attenuated Total Reflectance- Fourier Transform Infra-Red (ATR-FTIR) and X-Ray Diffractometer (XRD) (PANalytical X' Pert PRO) analyses were performed.

The microhardness tester (Zwick/Roell ZHU-5030) was used to measure micro hardness at the periphery of the irradiated Zn.

3 Results and discussion

3.1 SEM analysis

SEM images in Figs. 1a–l exhibit the variation in the surface morphology of ablated regions of Zn targets, exposed to 1000 laser pulses of pulse duration 30 fs in air, at various fluences of (a) 1.3 J cm^{-2} , over all view (b) 1.3 J cm^{-2} , centre (c) 1.3 J cm^{-2} , periphery (d) 2.5 J cm^{-2} , over all view (e) 2.5 J cm^{-2} , centre (f) 2.5 J cm^{-2} , periphery (g) 3.8 J cm^{-2} , over all view (h) 3.8 J cm^{-2} , centre (i) 3.8 J cm^{-2} , periphery (j) 5 J cm^{-2} , over all view (k) 5 J cm^{-2} , centre (l) 5 J cm^{-2} , periphery.

It is observed from above micrographs that in case of ablation in air, the circular craters are formed at all fluences in overall views. The area of crater increases with increasing fluence. The images in (Fig. 1 g and j) suggest that the protruding rim in the inner boundary of crater is formed for higher fluence of 3.8 J cm^{-2} and 5 J cm^{-2} . For the maximum fluence of 5 J cm^{-2} , the appearance of conical microstructures in the center of crater is clearly seen. In enlarged views of center as well as periphery, there is a non-uniform surface with an appearance of both micro and nanoscale droplets, ripples, pores, particulates and rims. In the central ablated areas, the distinct appearance of small scale droplets and ridges with very large number density is clearly seen at the lowest fluence of 1.3 J cm^{-2} (Fig. 1b). When the fluence is increased to 2.5 J cm^{-2} , the size of droplets increases significantly with a decrease in their number density (Fig. 1e). These structures merge together with increasing fluence and form multiple ablative layers and agglomerates rather than droplets (Fig. 1 h and k). In the peripheral ablated areas, the size of droplets is smaller and both their distinctness as well as number density are higher as compared to central ablated areas due to less energy deposition. The most distinct and highest number density droplets are observed at the lowest fluence of 1.3 J cm^{-2} (Fig. 1c). Increasing fluence results in increase in size and decrease in distinctness of the structures (Fig. 1f, i and l).

SEM images in Fig. 2a–l reveal the variation in the surface morphology of ablated regions of Zn targets, exposed to 1000 laser pulses of pulse duration of 30 fs in ethanol, for various fluences of (a) 1.3 J cm^{-2} , over all view (b) 1.3 J cm^{-2} , centre (c) 1.3 J cm^{-2} , periphery (d) 2.5 J cm^{-2} , over all view (e) 2.5 J cm^{-2} , centre (f) 2.5 J cm^{-2} , periphery (g) 3.8 J cm^{-2} , over all view (h) 3.8 J cm^{-2} , centre (i) 3.8 J cm^{-2} , periphery (j) 5 J cm^{-2} , over all view (k) 5 J cm^{-2} , centre (l) 5 J cm^{-2} , periphery.

In the central ablated areas, nanoscale colloids, dot-like elliptical conical structures with the highest number density are observed at the lowest fluence of 1.4 J cm^{-2} (Fig. 2b). When fluence is enhanced, the density of conical dot-like structures decreases significantly and number density of pores is considerably increased at the fluences of 2.5 J cm^{-2} (Fig. 2f). With further increase in fluence up to 3.8 J cm^{-2} , channels and bowl-shaped cavities are formed in Fig. 2h. At the maximum fluence of 5 J cm^{-2} , the only visible feature in Fig. 2k is an appearance of well-defined bowl-shaped cavities with very large number density. Some of these bowl-shaped cavities are ruptured with appearance of porous structures. In the peripheral ablated areas, at the lowest fluence, pores with very large number density along with appearance of unorganized channels are seen in Fig. 2c. When the fluence is increased to 2.5 J cm^{-2} (Fig. 2f), distinct and well-defined dot-like conical structures are observed. Significantly unorganized, undefined

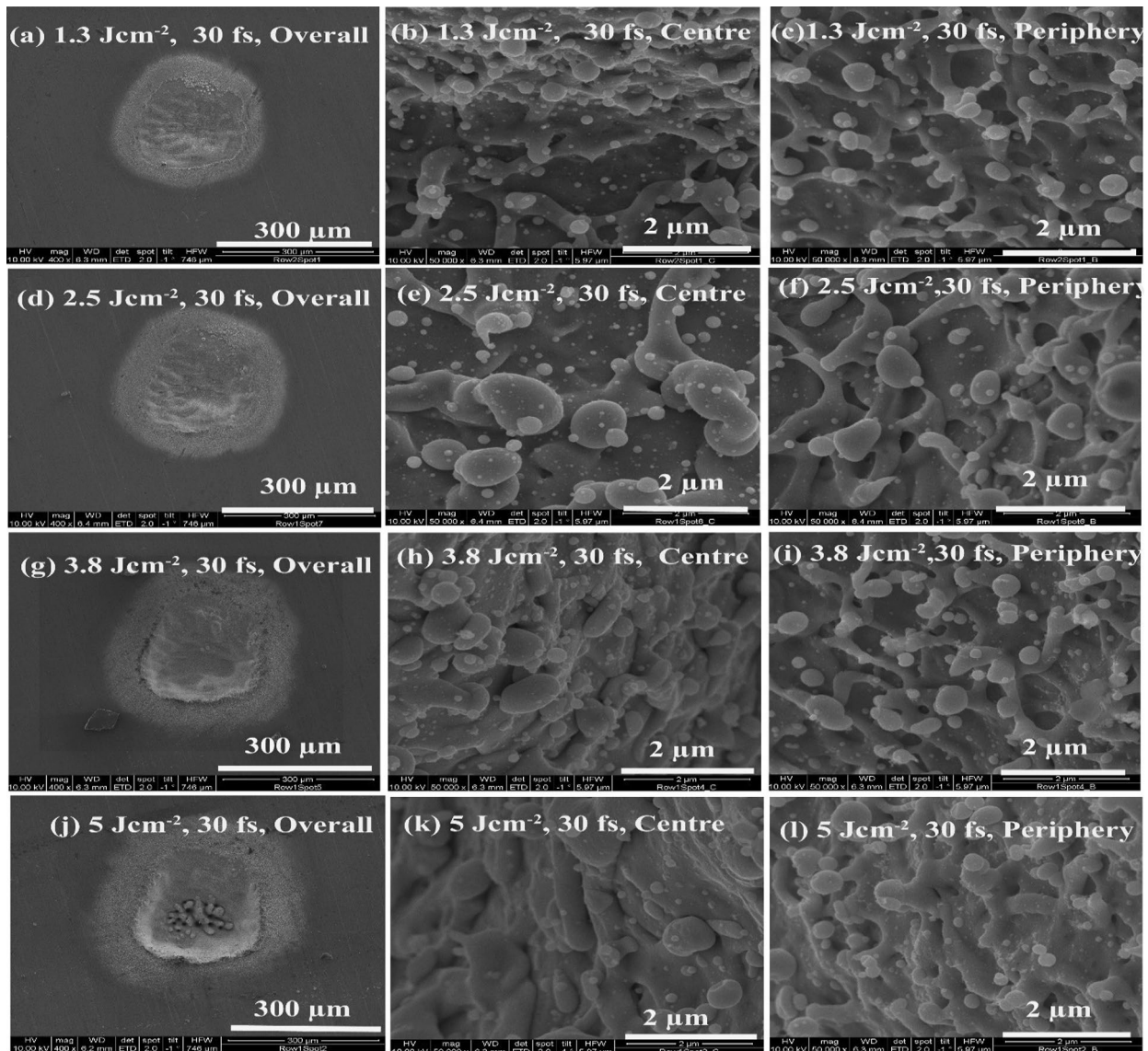


Fig. 1 SEM images showing the variation in the surface morphology of ablated regions of Zn targets, exposed to 1000 laser pulses of pulse duration 30 fs in air, at various fluences of **a** 1.3 J cm^{-2} , over all view **b** 1.3 J cm^{-2} , centre **c** 1.3 J cm^{-2} , periphery **d** 2.5 J cm^{-2} , over all

view **e** 2.5 J cm^{-2} , centre **f** 2.5 J cm^{-2} , periphery **g** 3.8 J cm^{-2} , over all view **h** 3.8 J cm^{-2} , centre **i** 3.8 J cm^{-2} , periphery **j** 5 J cm^{-2} , over all view **k** 5 J cm^{-2} , centre **l** 5 J cm^{-2} , periphery

and broken ripples or Laser-induced Period Surface Structures (LIPSS) with pores of significantly enhanced density are grown when fluence is enhanced to 3.8 J cm^{-2} (Fig. 2i). When the fluence is increased to a maximum values of 5 J cm^{-2} (Fig. 2l), the LIPSS become more organized and bifurcated.

The overall comparison of Fig. 1a, d, g, i with Fig. 2a, d, g, i suggests that the ablation depth of Zn in air is more pronounced than ethanol. Whereas, ablated areas are larger in ethanol than air.

The larger diameters and smaller ablation depth in ethanol assisted ablation of Zn than in air is explained below:

The adiabatic cooling, incident radiation loss due to scattering from chunk/nanoparticles emitted from the target surface and the dissociation of ethanol molecules hinder the laser energy reaching to the target surface. As compared to the air, more energy of incoming laser pulses is shielded in the ethanol because of the nanoparticles-related shielding effects, which reduce the removed materials and ablation depth of Zn in ethanol than in air. This is also possible reason of larger ablation threshold fluence of Zn in ethanol than air (by ablation rate and volume ablation rate methods).

The significantly lower value of thermal conductivity of air ($0.02435 \text{ W mK}^{-1}$) than ethanol (0.167 W mK^{-1}) also

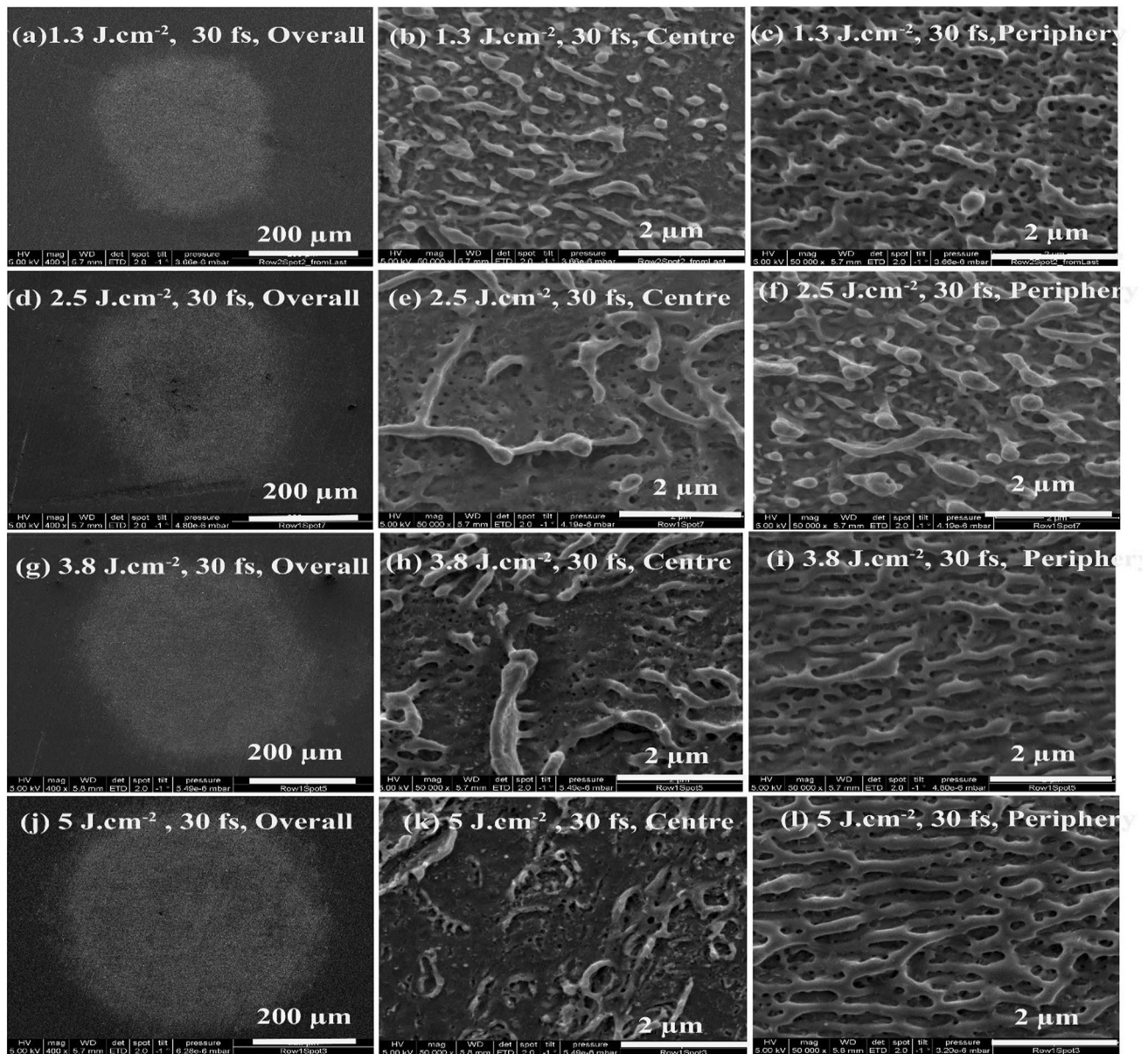


Fig. 2 SEM images showing the variation in the surface morphology of ablated regions of Zn targets, exposed to 1000 laser pulses of pulse duration 30 fs in ethanol, for various fluences of **a** 1.3 J cm⁻², over all view **b** 1.3 J cm⁻², centre **c** 1.3 J cm⁻², periphery **d** 2.5 J cm⁻², over

all view **e** 2.5 J cm⁻², centre **f** 2.5 J cm⁻², periphery **g** 3.8 J cm⁻², over all view **h** 3.8 J cm⁻², centre **i** 3.8 J cm⁻², periphery **j** 5 J cm⁻², over all view **k** 5 J cm⁻², centre **l** 5 J cm⁻², periphery

supports the lower thermal conduction losses and more sustainability of Zn plasma in air than in ethanol and hence causes increased ablation depth in air than in ethanol.

The laser beam radius (ω_f) after focusing through a 20 cm focal length lens is calculated using following formula.

$$\omega_f = \frac{\lambda f}{\pi \omega_0} = \frac{800\text{nm} \times 20\text{ cm}}{3.14 \times 0.75\text{ cm}} = 7\mu\text{m} [7\mu\text{m} \times M^2] \quad (2)$$

where λ is the laser wavelength, f is focal length of the lens, ω_0 is the beam radius without focusing and

$$M^2 = \theta / \frac{\lambda}{\pi \omega_0} = 2 \text{ is the beam quality factor or beam propagation factor} \quad (3)$$

Therefore, $\omega_f = 14\mu\text{m}$ (focused beam radius).

The slight increase in focal length will be responsible for larger ablation diameters in liquids as compared to air. This increase becomes more prominent for ablated areas generated with 1000 overlapping pulses.

The Rayleigh length (Z_R) is calculated as follows

$$z_R = \frac{\pi \omega_0^2}{\lambda} = \frac{3.14 \times 14 \mu\text{m} \times 14 \mu\text{m}}{800 \text{ nm}} = 0.7693 \text{ mm} \quad (4)$$

For irradiation, targets were placed at an optimized distance of 2.7 mm from the focus point.

Therefore, the beam radius ($\omega(z)$) at 2.7 mm from the focal point is

$$\omega(z) = \omega_f \left[1 + \frac{z^2}{z_R^2} \right] = 14 \left[1 + \left(\frac{2.7}{0.7693} \right)^2 \right]^{\frac{1}{2}} = 51 \mu\text{m} \quad (5)$$

where Z = distance of the target from focus point, Z_R = Rayleigh length.

Considering the different focal conditions in air and ethanol due to refractive index effects, the position of focal plane are adjusted by moving the sample along the optical axis to obtain the same focal positions in the experiments. For air experiments, a series of craters ($E_p = 50\text{--}450 \mu\text{J}$, $N = 1000$) were produced on the sample surface under different focal conditions and the focal plane was determined by finding the smallest diameter of the craters. Then we defined this position of focal point as $z=0$, where z is the position of z -axis (optical axis). In ethanol-assisted ablation, the focal planes were determined by the same method. The focal plane for ethanol experiments was 2.6 mm. The increase of focal length is resulted from a larger refractive index of ethanol (1.3617) than air (1.00).

Liquid-assisted ablation changes the focal length. When laser radiation undergoes through a liquid, a phenomenon of refraction occurs due to change of medium. The variation in the focal length is calculated as follows [28]

$$\Delta f = l \left(1 - \frac{1}{n} \right) \quad (6)$$

where l is the thickness of the layer and n is the refractive index of the liquid. By substituting the value of 10 mm as the thickness of ethanol and $n = 1.3617$ as refractive index of ethanol, Δf slightly increases to a value of 0.2648 cm.

The difference of the ablated diameters of Zn between two types of processing environments is related to the refractive index effects (the refractive index of air and ethanol is 1.00, and, 1.3617, respectively).

The enhancement of the ablation depths in air than ethanol is related to the different optical properties at the interfaces of transparent mediums and the Zn metal.

The optical Kerr effect is a phenomenon in which an electric field is due to the light itself and it causes a variation in index of refraction which is proportional to the local irradiance of the light. This refractive index variation is responsible for the nonlinear optical effects of self-focusing, self-phase modulation and modulational instability.

In ethanol-assisted irradiations, the laser is reflected at both air/liquids and liquids/Zn interfaces. Whereas, in air,

the reflection only occurs at air/Zn interface. The energy loss caused by the interfacial reflection has been evaluated. The reflection coefficient R for the incident laser at interfaces is evaluated using following relation [29]

$$R = \frac{(n - n_0)^2 + k^2}{(n + n_0)^2 + k^2} \quad R_{\text{air}} = 0.68 \text{ and } R_{\text{ethanol}} = 0.6009 \quad (7)$$

And $n = 2$ and $k = 4$ are the real and the imaginary part of the refractive index of the Zn target, $n_0 = 1$ for air and 1.3617 for ethanol is the refractive index of the ambient medium. At air/ethanol interfaces, considering $k = 0$ for liquid, R is calculated to be 2.3×10^{-2} for the air/ ethanol interface. At medium/Zn interfaces, n and k for Zn ($\lambda = 800 \text{ nm}$, 300 K) are 2 and 4, and the reflection coefficient comes out to be $R = 0.68$, and 0.6009 for air and ethanol ambiances, respectively. Therefore, for the same incident laser fluence, the reflection-induced energy loss in ambient air is 13% higher than ethanol. Therefore due to more energy deposition into the sample surfaces in ethanol, resulting in the decrease of the ablation threshold fluence (by D^2 method) and enhanced ablation diameters of Zn than in air.

Furthermore, the enhanced recoil pressures of the laser induced shockwaves and bubble-related mechanical forces under liquid confinements would also cause the extra damage of the sample [22]. It is responsible to reduce the threshold fluences and increase in the ablated areas. Laser ablation at solid-liquid interface includes interaction between laser light and the target, which creates localized high temperature and pressure plasma plumes above the target surface. Berthe et al. [30] reported that the plasma-induced pressure level reaches to 2–2.5 GPa when 1–2 GW/cm² irradiance from a 308 nm XeCl excimer laser with 50 ns pulse width was used to ablate an Al target in water. Under this high temperature and pressure several chemical reactions and physical processes, that are not possible at normal conditions, will take place among ablated species and solvent molecules enhance ablated areas in liquids than air.

The plasma-induced plasma effects are also more pronounced in liquids than air due to restriction of free expansion of ablated species. This is called confinement effect which is attributed to 655 times higher density of ethanol (789 kg m⁻³) than air (1.2041 kg m⁻³), smaller ionization potential of ethanol 10.47 eV than air components i.e. N₂ (15.5 eV) and O₂ (12 eV) CO₂ (13.79 eV).

The craters with uplifted rims are formed in air whereas, ablation in ethanol is cleaner without melt expulsion and redeposition. Similarly, the comparison of enlarged views of central and peripheral ablated areas in Figs. 1b, c, e, f, h, i, k and l and 2b, c, e, f, h, i, k and l clearly shows that the size of all kinds of nanostructures is significantly

smaller in ethanol as compared to that in air. This is the clear indication that wet ablation regardless of the fluence is more suitable for the growth of fine nanoscale structures.

The laser-induced surface structuring of materials strongly depends upon the ablation yields, kinetic energies and densities of electron and ions of generated plasma plume which can be controlled by controlling three factors (1) laser parameters (fluence, wavelength, number of pulses and pulse duration), (2) nature of material and (3) environmental conditions. The main decisive parameters whose distribution and profile in time and space defines shape, growth and size of surface structures are (1) energy deposition to the target material, (2) temperature, pressure, and density gradients of ablated plume and shock pressure, (3) density and K.E of ions/electrons of laser-ablated plasma, (4) mass/density/refractive index, pressure and ionization potential of environment, (5) reflection, absorption, melting point and threshold fluence of ablated target material.

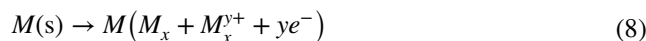
Laser-produced plasma in liquid environment creates thermodynamic state of high temperature, high pressure and high density, which is a favorable condition for the formation of metastable phases [31]. Therefore, liquid medium plays a crucial role in the formation of smaller sized structures. An extended plasmonic thin film model successfully explains the reduced size of structures in ethanol than air. The channels like ripples with average diameter of 200 nm are obtained after irradiation of Zn in ethanol and originate from surface plasmon polariton excitation in the presence of a thick Zinc oxide layer (with thickness greater than native layer), while the optical excitation of ethanol also plays an important role [32].

A possible explanation for this fact are confinement effects of ethanol which prevents the free expansion of the plume and random movement of ejected material during laser ablation and serves for the fixation of surface waves, in a well-defined manner. The enhancement in the thermal energy coupling to the target in denser medium also causes break up of larger structures into smaller ones [33]. The growth of smaller structures in liquids is also attributed to the nucleation and condensation of vapor w due to surface instability or recoil pressure from the expanding vapor plume.

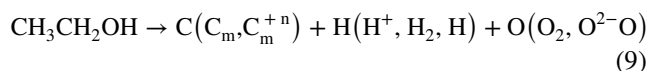
The laser interaction with metallic targets in organic solvent (ethanol) is beneficial for the nucleation and the growth of metal carbides [4], while the subsequent carbon precipitation on the carbide particles facilitates the formation of carbon-encapsulated core – shell nanostructures. The carbon solubility in metals and the reactivity of the target metals play a critical role in the formation of cores, while metal-catalyzed carbonization determines the state of the carbon shells with different crystallization rates. Ethanol (C₂H₅OH or CH₃CH₂OH)-assisted ablation of Zn is responsible for

the formation of mixtures of M@C and MO_x@C, whereas, the formation of metal (Zn) carbides is not reported [34].

When high intensity laser pulses interact with a metal target, a plasma with high temperature (> 5000 K), high pressure (> 1 GPa), and high density is generated [35], which immediately causes the ionization and the atomization of the ablated metals to generate metal plume species [34].



Simultaneously, laser-induced decomposition of the organic solvent molecules also takes place during the ionization /atomization of the ablated metals [35], leading to the formation of a large amount of freely active carbon atoms/clusters, hydrogen and oxygen gases and radicals and carbon-based fragments, following the reaction of Eq. 9 [34]



The expanding plasma plume under highly confined environment ionizes ethanol molecules at plasma-ethanol interface, which may be termed as plasma induced plasma. Laser-produced plasma have ionized species from target materials, while plasma-induced plasma consists of ionized species from ethanol molecules. Cationic species such as Zn⁺ from laser-produced plasma react with the anionic species such as O⁻ or OH⁻ from plasma-induced plasma at plasma liquid interface to generate oxide/hydroxide molecules under highly non-equilibrium environment. The as produced molecules get rapidly quenched into particles and may have the possibility of having some un-reacted cations/anions/neutral atoms or their vacancies into the lattice [36]. In the plasma phase, when metal ions or atoms react with the species generated from the decomposition of ethanol molecules, metal carbonization and metal oxidation takes place. The plasma will quench within hundreds of nanoseconds, and in this duration the temperature and pressure of environment sharply decline, facilitating the formation of droplets, pores and colloids.

For the metals with non d-vacancies in their outer electron configuration, such as Zn (d¹⁰s²), the metals in the molten state show a negligible affinity for carbon. For metallic Zn, the carbon solubility is approximately zero at the molten state (600 – 700 °C); thus, no metal carbides, such as ZnC_x, form in the products. The formation of ZnO is attributed to the higher affinities of Zn to O atoms than C atoms to form oxide (confirmed by FTIR and XRD analyses both Figs. 11a, b and 12). The oxygen may come from the split of C-O bonding of the ethanol molecules or the dissolved oxygen gases in ethanol. The carbon has low solubility in the oxide particles so that it precipitates on the surfaces of oxide particles to construct carbon shells [34]. Liquid-Assisted Laser ablation (LAL)-induced decomposition of organic molecules

may also generate many organic byproducts, such as enol and enol complex (confirmed from FTIR analysis Fig. 11c). These particulates are inhibited, leading to the formation of small structures, much smaller than those synthesized by laser ablation in air. Metal oxide (ZnO) suggests the presence of oxygen which indirectly supports the reduction of oxide particles or carbonization of oxide into pure metals or pure carbides by reductive gases (H_2 , CH_4 , CO) in the gas (bubble) phase. When the particles are released into the liquids after the bubble collapses, carbon precipitation and subsequent laser-irradiation-triggered “metal-catalyzed graphitization” leads to the formation of onion-like carbon shells [34]. The liquid-assisted ablation plays an important role in the growth, ripening and aggregation of smaller nuclei after Zn/ZnO core shell structures. These structures are originated from molten droplet formed via explosive boiling of the target, and the subsequent oxidation of these particles forms the oxide shell and bi-layer micelle [37].

Figure 3 exhibits different marked regions of laser-ablated crater on the surface of Zn when it is exposed to 1000 laser pulses in ethanol at a fluence of 2.5 J cm^{-2} , with pulse duration of 30 fs. (a) overall ablated crater with different regimes, (b) enlarged view of central ablated area with wrinkled surface and channels, (c) enlarged view of central ablated area of ‘b’ with channels, micro and nanoscale colloids, droplets and pores, (d) enlarged view of central ablated area of ‘c’ with nanoscale colloids, droplets and pores, (e) enlarged view of inner boundary with wrinkles and cones, (f) enlarged view of inner boundary of ablated area ‘e’ with

dot-like conical structures and droplets, (g) enlarged view of inner boundary ablated area ‘f’ with distinct and well-defined dot-like conical structures, (h) enlarged view of outer boundary with broken channels, pores and indistinct cones, (i) enlarged view of outer boundary ‘h’ with broken channels and pores.

The detailed FESEM images of different regions of fs-laser ablated spot of Zn are shown in Fig. 4a–j in air. Figure 4a represents the entire crater, whereas, SEM images in Fig. 4b–d on LHS show enlarged views of central ablated areas at various magnifications with spider net like structures. Inner boundaries are shown on the RHS in SEM images of Fig. 4e, f with dot-like structures and particulates. Outer most boundaries (lower sections) of ablated crater on the surface of Zn in air are enlarged in the lower portion of SEM images in Fig. 4h–j. It is observed that organized LIPSS formation is only observed in air, in the outmost boundaries.

These Figs. (3, 4) clearly reveal that LIPSS formation is only observed in air Fig. 4h–j, whereas, in ethanol, the surface of fs laser-ablated Zn shows no LIPSS formation. However, some unorganized and broken ripples or channels are clearly seen whose periodicity is difficult to evaluate (Fig. 3f, i). The structures which are grown in ethanol (Fig. 3h, i) are actually channels with average diameter of 200 nm. The formation of nanocavities is also observed with a diameter ranging from 50 to 200 nm.

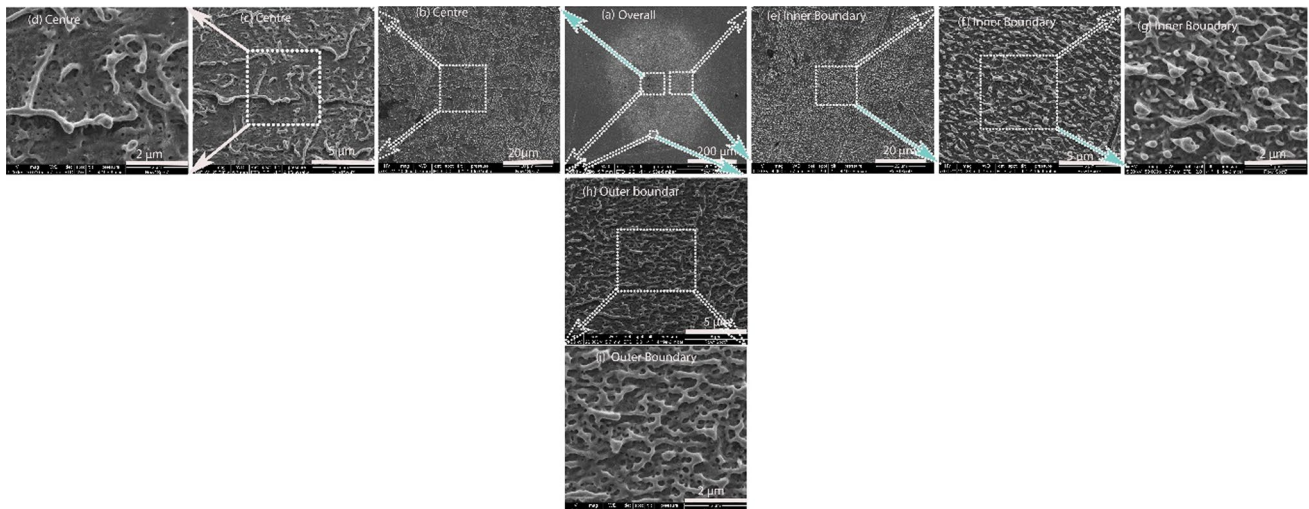


Fig. 3 Different marked regions of laser-ablated crater on the surface of Zn when it is exposed to 1000 laser pulses in ethanol at a fluence of 2.5 J cm^{-2} , with pulse duration of 30 fs. **a** overall ablated crater with different regimes, **b** enlarged view of central ablated area with wrinkled surface and channels, **c** enlarged view of central ablated area of ‘b’ with channels, micro and nanoscale colloids, droplets and pores, **d** enlarged view of central ablated area of ‘c’ with nanoscale

colloids, droplets and pores, **e** enlarged view of inner boundary with wrinkles and cones, **f** enlarged view of inner boundary of ablated area ‘e’ with dot-like conical structures and droplets **g** enlarged view of inner boundary ablated area ‘f’ with distinct and well-defined conical structures, **h** enlarged view of outer boundary with broken channels, pores and indistinct cones, **i** enlarged view of outer boundary ‘h’ with broken channels and pores

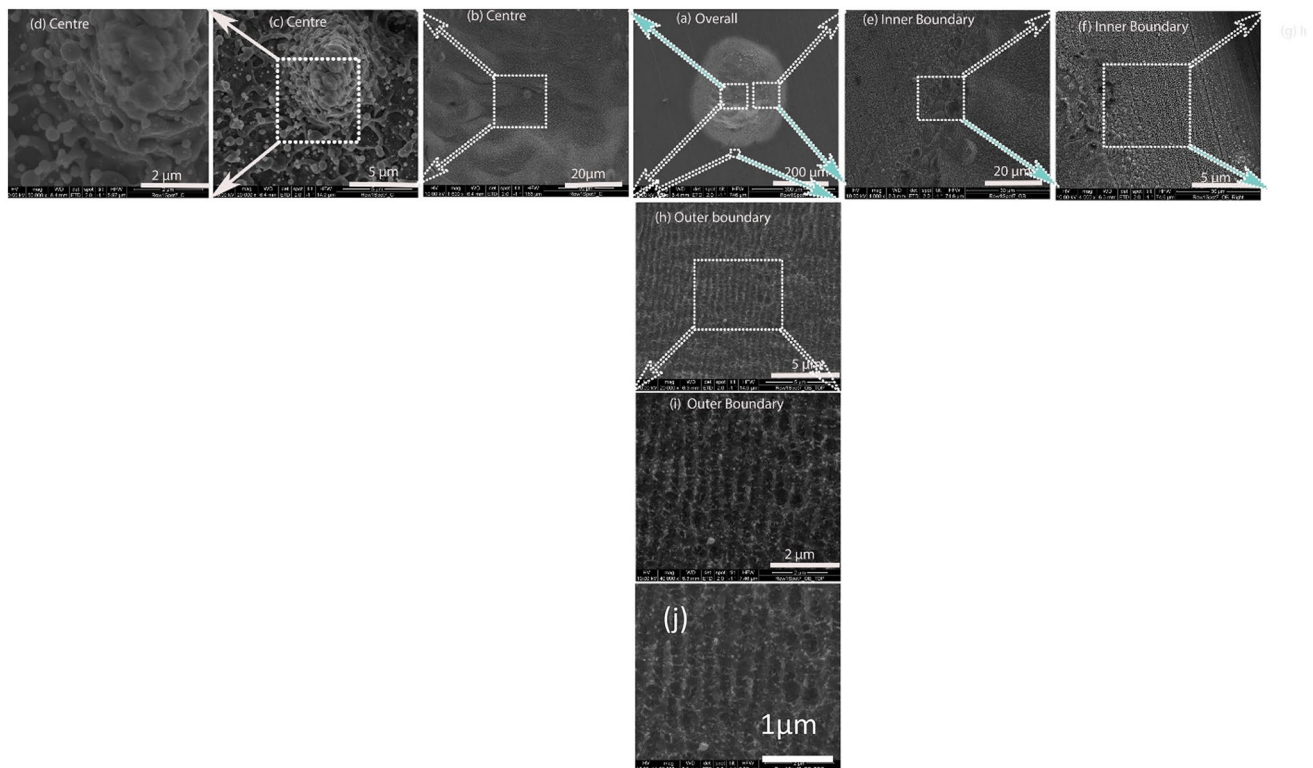


Fig. 4 The detailed FESEM images of different regions of fs laser-ablated spot of Zn are shown in **a–j** in air. **a** Represents the entire crater, whereas, SEM images in **b–d** on LHS show enlarged views of central ablated areas at various magnifications with spider net-like structures. Inner boundaries are shown on the RHS in SEM images

of **e, f** with dot-like structures and particulates. Outer most boundaries (lower sections) of ablated crater on the surface of Zn in air are enlarged in the lower portion of SEM images in **h–j**. Organized LIPSS formation is only observed in air, in the outmost boundaries

To explore the formation of LIPSS at the peripheries of the central ablated craters, the values of local fluences have been estimated using Eq. 1 [38].

$$F_{\min} \approx F_{\text{peak}} \exp \left[-1/2 \left(\frac{D_{\text{LIPSS}}}{\omega_0} \right)^2 \right] \quad (10)$$

where is F_{\min} is the local fluence, F_{peak} is the peak fluence, D_{LIPSS} is diameter of peripheral region (200 μm for present case, where the growth of LIPSS is observed), ω_0 is the beam waist. The value of the peak fluence ranges from 0.6 J cm^{-2} to 5.7 J cm^{-2} and local fluence ranges from 0.2 to 1.9 mJ cm^{-2} . A significant drop of the fluence range is seen from the center to the periphery of the craters. The evaluated values of local fluences are 0.2, 0.4, 0.6, 0.8, 1, 1.3, 1.5 and 1.7 mJ cm^{-2} .

SEM images of Fig. 5 represent the outermost peripheral ablated area of Zn after exposure to 1000 pulses in air at pulse duration of 30 fs, where Laser-Induced Periodic Surface Structure (LIPSS) are grown at various local fluences of (a) 0.4 mJ cm^{-2} , (b) 0.8 mJ cm^{-2} , (c) 1.1 mJ cm^{-2} and (d) 1.5 mJ cm^{-2} . The average periodicity of LIPSS on the surface of fs laser-ablated Zn in air varies from 500 ± 5 to 860 ± 5 nm

in SEM images of Fig. 5a–d. These are LSFL whose generation can be attributed to the interaction of the incident laser beam with a surface electromagnetic wave (SEW) generated at the rough surface, which might include the excitation of surface plasmon-polaritons (SPP) [39]. The orientation of these kind of structures is usually observed perpendicular to the polarization. But in our case, we have not considered the direction of polarization.

The most distinct, organized and fine ripples are grown at the lowest fluence of 0.2 mJ cm^{-2} (Fig. 4a). When the fluence increases, the energy deposition to Zn target increases which is responsible for the extensive melting and vanishing of the LIPSS at the highest fluence (Fig. 4d).

The periodicity of LIPSS has been plotted as function of local fluence in graph of Fig. 6a. This graph shows that the periodicity of ripples increases with the increasing fluence which is attributed to more energy deposition per atom which is shown in Fig. 6b LIPSS periodicity is difficult to measure for Zn ablation in ethanol. Okamuro et al. [40] also reported that the grating spacing of periodic structures self-formed on the surface of several metals under femtosecond laser-pulse irradiation depends upon the laser fluence. This dependence is the same for all metals, although the range

Fig. 5 SEM images exhibiting the outermost peripheral ablated area of Zn after exposure to 1000 pulses in air at pulse duration of 30 fs where Laser-induced Periodic Surface Structures are grown at various local fluences of **a** 0.4 mJ cm^{-2} , **b** 0.8 mJ cm^{-2} , **c** 1.1 mJ cm^{-2} and **d** 1.5 mJ cm^{-2}

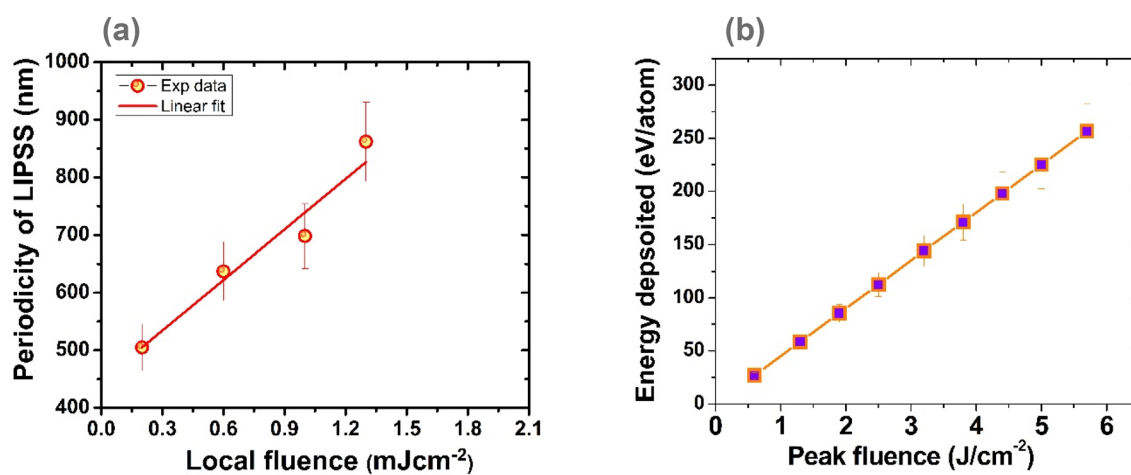
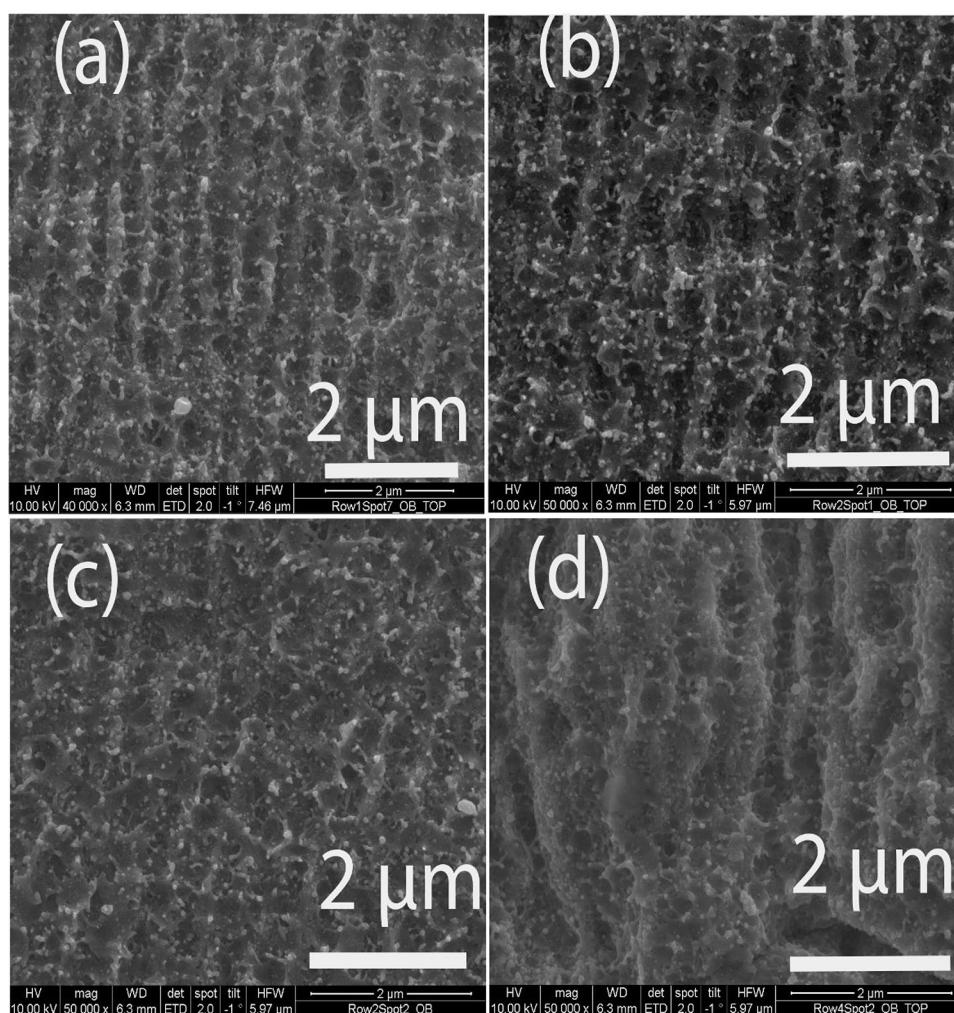


Fig. 6 **a** The periodicity of LIPSS formed on the surface of fs laser-ablated Zn in air as a function of local fluence. **b** The energy deposited (eV) per Zn atom as a function of peak laser fluence

of laser fluence in which the structures are formed differs between metals. The laser fluence dependence is explained on the basis of parametric decay model [41] of laser light. According to this model, the formation of periodic structures depends not only on metal properties but also on the electron density of plasma produced on a surface by femtosecond laser pulses.

The parametric process of photon \rightarrow photon + plasmon occurs on a plasma surface as well as in a bulk plasma, i.e., Stimulated Raman Scattering. The parametric conditions of $\omega_L = \omega_2 + \omega_{sp}$, where the subscripts L, 2, and SP indicate the incident laser light, scattered light, and surface-plasma wave, respectively, are reduced to $\omega_L - \omega_{sp} = c k_{sp} - c k_L$ where $\omega_L = c k_L$ and $\omega_{sp}^2 = c^2 k_{sp}^2 + \frac{1}{2} \omega_p^2 - \sqrt{c^2 k_{sp}^4 + \frac{1}{4} \omega_p^4}$.

The wave number of the plasma wave induced by the parametric process can be related to the plasma frequency, which is directly proportional to electron density.

The LIPSS formation is generally attributed to interaction of the incident laser beam with the excited surface plasmons [42, 43].

During laser matter interaction, the formation of LIPSS depends upon the laser fluence, nature of material and environmental conditions.

For the formation of LIPSS there is a specific window or range of specific laser fluences which depends upon the nature of each material. If the fluence is below the range of threshold fluence, it will not be able for the significant enhancement of local field and no surface plasmons—polaritons interactions are possible due to low electron temperature and density of plasma. If the fluence is significantly higher than a certain range, then LIPSS are destroyed or can become unorganized and undistinguished. Some times larger structures are broken into smaller grains or substructures. Therefore the reason why LIPSS are not formed in ethanol? Is explainable on the basis of (1) significantly enhanced local electric field due to more energy deposition in ethanol than in air, (2) significantly enhanced chemical reactivity of ethanol than air, (3) larger impulse, ablation pressure and shock pressure due to longer life time of shock waves in ethanol than in air.

(1) Significantly enhanced local electric field due to more energy deposition in ethanol than in air.

A possible explanation for this fact are confinement effects of ethanol which prevents the free expansion of the plume and random movement of ejected material during laser ablation and serves for the fixation of surface waves, in a well-defined manner. The enhancement in the thermal energy coupling in denser medium also causes to more energy deposition in ethanol than in air [33].

When the material is irradiated by a focused femtosecond laser beam, multiphoton absorption and photoionizations occurs. Thus, the electron plasma is created in the material,

characterized by the electron plasma temperature (T_e), and the plasma density (N_e). An analytical expression for the periodicity (Λ) of LIPSS versus electron temperature (T_e), and density (N_e) proposed by Shimotsuma et al. [44] is as follows

$$\Lambda = \frac{2\pi}{\sqrt{\frac{1}{T_e} \left(\frac{m_e \omega^2}{3k_B} - \frac{e^2 N_e}{3\omega k_B} \right) - k_{pp}^2}} \quad (11)$$

where m_e is electron mass, k_B is the Boltzmann constant, ω is the angular frequency.

LIPSS formation is attributed to the excitation of surface plasmon polaritons to induce the periodic enhancement of local fields in the surface layer. Upon fs-laser irradiation in air or especially in ethanol environment, the irregular damage at specific sites (being indicative of Kerr-effect-mediated filamentation) and the superficial oxidation at the irregular damage sites (as revealed by FTIR and XRD analyses both) play vital role for such kind of surface nanostructuring. This causes breakup of laser beam upon propagation through very thick ethanol layer above the Zn sample [32]. As a result, there are hot spots or regions of increased localized fluence which exceeds the ablation threshold fluence of the Zn whereas, there are some regions where fluence is smaller than ablation threshold fluence. The ethanol above the hot spots will also be strongly excited and may change its optical properties transiently during the fs-laser pulse. Moreover, upon multi-pulse irradiation, the ablated Zn surface oxidizes, resulting in an oxide layer thickness exceeding that of the native oxide (> 3 nm) [32].

(2) Significantly enhanced chemical reactivity of ethanol than air.

The ablated Zn surface undergoes chemical modifications in both air and ethanol, for instance, ablation of Zn in air may produce oxidation such that the LIPSS are constituted by ZnO rather than just metallic Zn. However, oxide formation of Zn in ethanol is more pronounced than air (confirmed by FTIR and XRD analyses of Figs. 10a, b and 11). But LIPSS formation is more pronounced in air than ethanol. Therefore, LIPSS formation cannot be completely explained on the basis of oxide or on the basis of plasmonic model. Several models can be proposed to explain the formation of sub- or super wavelength LIPSS of scale 0.62λ to 1.125λ in air or channels of dimensions 0.25λ in ethanol on Zn surface after ablation. Miyaji et al. [45] suggested a standing plasmonic wave model with parametric study and proposed that individual surface plasmon-modes at the interface of a highly laser-excited target interlayer between the surrounding liquid plays significant role for the growth of such nanostructures. Ethanol-assisted ablation-induced decomposition of organic molecules may also

generate many organic byproducts, such as enol and enol complex (confirmed from FTIR analysis Fig. 11c). These products are absent in case of air-assisted ablation.

In the presence of liquids, the chemical reactivity of the target with liquid is significantly enhanced which is responsible for the growth of new phases and modification in the chemical composition of the irradiated target. Four kinds of chemical reactions would take place at the interface between the liquid and the laser-induced plasma [46]. The first kind of chemical reactions take place inside the high temperature and high pressure laser-induced plasma and are responsible for metastable phase. The second kind of chemical reaction occurs between the reactant species from the target and the liquid, after its excitation and evaporation. The third set of chemical reactions occur at the interface between the laser-induced plasma and the liquid. It happens because the thermodynamic state with high temperature, high pressure and high density of the laser-induced plasma provides a good opportunity to the high-temperature chemical reactions between the ablated species from the target and the molecules of the liquid. The fourth kind of chemical reaction occurs inside the liquid. The extremely high pressure in front of the laser-induced plasma will impinge the ablation species from the solid target at the plasma–liquid interface into the liquid, and then, the chemical reactions between the ablation species and the liquid molecules will occur inside the liquid. Therefore, these chemical reactions support the fabrication of new materials by the combination of the elements of the target and the liquid [46].

(3) The larger impulse, ablation pressure and shock pressure due to longer life time of shock waves in ethanol than in air.

Laser ablation is accompanied by direct laser ablation and laser-induced shock waves generation. The ambient conditions (composition, temperature, and pressure of the environment in which the breakdown occurs) affect the hydrodynamic expansion features of the laser plasma explosion greatly. The shock waves are generated at the interface between the plasma and ambient medium and will continue to expand. After decoupling of shock front from the plume, the reflected shock wave propagates rapidly back toward the plume, thereby halting further expansion of the plasma. The atomistic modeling results show that spatial confinement of the plume by shock wall reflection leads to an increase in local temperature and lifetime [47].

In ethanol, the confinement process increases the life time of shock waves [31], and when the laser is switched off, the plasma still maintains a pressure which decreases during its adiabatic cooling. During these two steps, the target acquires an impulse momentum due to the induced shock wave. The ethanol-assisted ablation of Zn due to the

confining process increases impulse, $\beta P_a(\tau)\tau$ by a factor “ β ” of the order of 5, and with a resulting ablation pressure “ P_a ” which is typically 4–10 times greater than in direct ablation in air [31].

LIPSS are formed on the surface of Zn in air environments, whereas, channel like structures are grown for Zn ablation in ethanol. It indicates that air is more favourable for the growth of LIPSS as shown in Figs. 4g, h and 5a–d than ethanol as shown in Fig. 3h–i. In ethanol, broken or unorganized ripples or channels are formed. The formation of regular periodic surface structures by multi-pulse laser irradiation of Zn under vacuum condition has also been reported previously [48].

In 2009, the theory of Sipe was combined with a Drude model for considering the optical response of the quasi-free conduction band electrons of the laser-excited solids [27]. This approach successfully describes LIPSS in ZnO and confirms the importance of transient changes of the dielectric permittivity during the early stage of LIPSS formation on semiconductors upon irradiation with ultrashort laser pulses [49].

The chemical reactions with the ambient environment, such as oxidation [21], incubation effects generating permanent defect states [50], reducing the damage thresholds, or self-organization promoting surface erosion and diffusion of atoms can be possible causes of such structures [26].

In summary, the ablated areas of Zn are larger in ethanol than air. Whereas, the ablation depth of Zn in air is higher than that in ethanol. The debris free clean surface of Zn after ablation in ethanol as compared to that in air is observed. Similarly, the wet ablation is more favorable to grow small scale nano structures as compared to ablation in the dry environment. However, distinct and well-organized LIPSS are formed in air, whereas, channel-like structures and nanocavities are formed in ethanol.

3.2 Analytical evaluation of ablation threshold

The ablation threshold is a key parameter for discussing the mechanism of surface structuring of material during laser ablation. The ablation of solid targets by femtosecond, picosecond and nanosecond laser irradiation has been investigated by Chichkov et al. [25] by presenting theoretical models and quantitative analysis of experimental results. Similarly, in another work, ablation of metals by ultrashort laser pulses has been reported by Nolte et al. [26]

Some important physical and thermal parameters of Zn which have been used for analytical evaluations are listed in Table 1 [21, 23, 50–53].

The threshold laser fluence for ablation of metals is defined by Gamaly et al. [50] according to the following expression

$$F_{th} = \frac{3}{8} (\epsilon_b + \epsilon_{esc}) \frac{\lambda n_e}{2\pi} \quad (12)$$

for short laser pulses, where $\epsilon_{esc} = 4.34$ eV/atom is the work function, ϵ_b is the binding energy, or heat of evaporation per atom with value 1.233 eV/atom, for Zn, λ is wavelength of irradiation (8×10^{-5} cm), n_e is the number density of conduction electrons (6×10^{22} cm $^{-3}$). Substituting these values in Eq. (12), a threshold fluence value of 0.2098 J cm $^{-2}$ is obtained.

The reported ablation threshold values in different studies show a large spread ranging from 0.022 to 1.8 J cm $^{-2}$, [23]. Since Zn is a transitional hexagonal close packed (hcp) metal with high Debye-Weller thermal parameter value B (or larger mean-squared amplitude of atomic vibration), the lower value of threshold fluence of Zn is expected [52].

The ablation threshold can be approximated by the enthalpy of evaporation per unit volume $\rho\Omega_{vap}$, by following expression [53]

$$F_{th} = \frac{\rho\Omega_{vap}}{\alpha A} \quad (13)$$

where A is absorption of light in Zn. The enthalpy of evaporation per unit volume is 12.75 GJ/m 3 . The analytical

value of threshold fluence using relation 12 is found to be 0.267 J cm $^{-2}$.

3.3 Ablation threshold by squared diameter vs. fluence

The second method for the evaluation of ablation threshold of solid materials is referred to as the D^2 method and is also the most reported and widely used method [21–23, 27, 55].

In this method, the diameter of ablated area or ablated crater after Zn ablation in both air and ethanol environment is explored by SEM analysis. A simple technique for measurements of pulsed Gaussian-beam spot sizes is reported by Liu [27]. This technique is particularly useful for measurements on highly focused beam spots. It can also be used for absolute calibration of the threshold-energy fluences for pulsed laser-induced effects.

With Gaussian distribution of laser beam, the crater diameter is expressed as follows [27, 56]

$$D = a \left\{ \ln \left(\frac{F}{F_{th}} \right) \right\}^{0.5} \quad (14)$$

Table 1 Some important thermal, optical and physical properties of Zn [21, 23, 50–53]

Frequency of 800 nm radiation (8×10^{-5} cm) (θ)	375 THz
Resistivity $\mu\Omega\text{m}$	0.059
Permeability	1
Optical penetration depth or skin depth (nm)	6.3
($L \alpha$) for 800 nm = $\left(\frac{1}{\alpha}\right)$	0.006313 μm
Absorption Coefficient (α) cm $^{-1}$	1.58×10^6
Energy deposited at a laser fluence of 2.5 J cm $^{-2}$ eV/atom	112
Number density of conduction electrons cm $^{-3}$	6×10^{22}
No of atoms of Zn cm $^{-3}$	6.603×10^{22}
Work function eV atom $^{-1}$	4.34
Binding energy or heat of evaporation per atom eV atom $^{-1}$	1.233
Heat of Vaporization KJ kg $^{-1}$	1,191,782 [21]
The enthalpy of evaporation per unit volume [54] $\rho\Omega_{vap}$ GJ m $^{-3}$	12.75
Density Kg m $^{-3}$	7140
Heat of fusion kJ mol $^{-1}$	7.322
Boiling point Celsius	907
Thermal conductivity W m $^{-1}$ K $^{-1}$	116
Specific heat J g $^{-1}$ K $^{-1}$	0.39
Thermal diffusivity ($\chi = \frac{K}{\rho c}$) cm 2 s $^{-1}$	0.4
Thermal diffusion depth (μm)	2
Refractive index for 800 nm (n) [23]	2
Extinction coefficient for 800 nm (k) [23]	4
Reflection coefficient for 800 nm (R) [23]	0.7
Absorption coefficient for 800 nm(A) [23]	0.3
Debye waller thermal parameter (B) related to the mean-square amplitude of atomic vibrations $\langle u^2 \rangle$ $B = \frac{8\pi^2 \langle u^2 \rangle}{3}$ nm 2 [52]	0.0145

$$\text{or } F_{th} = F \exp \left\{ - \left(\frac{D}{a} \right)^2 \right\} \tag{15}$$

where F is the peak fluence, F_{th} threshold laser fluence for ablation, D is the crater diameter, a is the laser beam diameter from the slope. However, the calculated beam diameter from the slope does not necessarily reflect the actual beam diameter, due to the change in absorption within the irradiated zone for multiple pulses or due to accumulation effects. The squared diameter D^2 of ablated crater on Zn after ablation with fs laser pulses in air and ethanol is plotted as a function of peak fluence on a semi-logarithmic scale in Fig. 7. This graph shows that squared diameter of ablated crater increases with increasing fluence logarithmically. The ablation threshold fluence of Zn, F_{th} is determined from a linear extrapolation to $D^2 = 0$.

The experimental values of ablation threshold fluence of Zn in ethanol and air for 1000 multiple pulses come out to be $F_{th, Zn, Ethanol} = 0.53 \text{ J cm}^{-2}$ and $F_{th, Zn air} = 1.0 \text{ J cm}^{-2}$. A larger value of ablation threshold of Zn, i.e., about two times higher in air than ethanol is observed.

It is observed that squared diameter of ablated crater increases with increasing fluence in both environments. However, in ethanol, the crater area is significantly larger as compared to that in air at all fluences. Confinement effects as well as significantly enhanced pressures and temperatures in liquids are the possible causes for the larger ablated areas and smaller threshold fluence value [4, 5, 19, 57, 58].

It is also observed that threshold fluence for Zn in ethanol is about two times smaller than in air. It is attributable to confinement effects offered by ethanol to Zn plasma. The incubation in liquid media generally increases in comparison with air [15]. The optical absorption mechanism also

increases at such large number of pulses due to alcoholic fluids with various carbon numbers. The influence of this carbon number on the incubation may suggest a possible increase in the absorptivity of the cavity surfaces due to carbonaceous deposits generated by laser-induced pyrolysis as has been reported previously by our group [4]. Therefore, for enhanced surface absorptivity of laser-pulsed energy and fine surface structuring, liquid-assisted ablation in a confined environment is preferable over dry environment.

3.4 Ablation threshold evaluation by ablation rate

A second method used to determine the ablation threshold fluence is based on the ablation rate in terms of crater depth per pulse. The relation between optical ablation depth L_{opt} , peak fluence F and threshold fluence F_{th} is derived from the Lambert–Beer law and can be described as follows [55]:

$$L_{opt} = \frac{1}{\alpha} \ln \left(\frac{F}{F_{th}} \right) \tag{16}$$

The skin depth for Zn is 6.3 nm (see Table 1).

Ablation rate per pulse ($\mu\text{m}/\text{pulse}$) for high fluence regime,

$$L_{high} = l_{th} \times \ln \frac{F}{F_{th}} \tag{17}$$

where $l_{th} \sim \sqrt{\chi\tau}$ is thermal diffusion depth for Zn. where $\chi = \frac{K}{\rho C}$, is thermal diffusivity $= 0.4 \text{ cm}^2 \text{ s}^{-1}$, K is thermal conductivity, i.e. $116 \text{ W m}^{-1} \text{ K}^{-1}$, ρ is density 7.14 g/cm^3 , and C is specific heat capacity of the Zn material $0.39 \text{ J g}^{-1} \text{ K}^{-1}$. By substituting the approximate value of electron–phonon coupling time of 10 ps for Zn, the approximate value of thermal diffusion depth comes out be $2 \mu\text{m}$. $\frac{F}{F_{th}}$ is ratio of peak fluence to threshold fluence. Minimal heat diffusion and absence of plasma shielding are the major features of fs laser-produced plasmas. The ejection of particles occurs from the target surface well after the arrival of the laser pulse, allowing efficient coupling of the laser energy to the target surface.

The experimental ablation threshold is determined by considering the experimental values of ablation depth to investigate the ablation rate dependence on the laser fluence. The ablation rate is determined using the following relation [25]

$$L = l \times \ln \frac{F}{F_{th}} \tag{18}$$

where L is ablation rate, l is ablation depth which is experimentally determined using confocal.

The ablation depth varies from 94 to 133 μm in ethanol and 104–146 μm in air with increasing fluence from 0.6 to 5.7 J cm^{-2} and is plotted in graph shown in Fig. 8. The

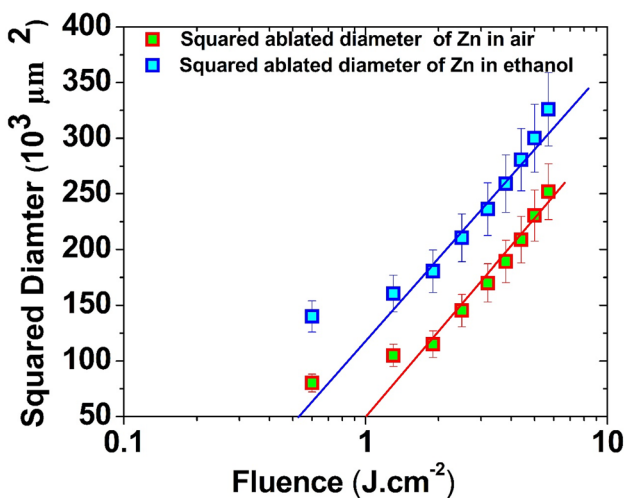


Fig. 7 The squared diameter D^2 of ablated crater on the surface of Zn after ablation with 30 fs and 1000 applied laser pulses in air and ethanol as a function of peak fluence on a semi-logarithmic scale

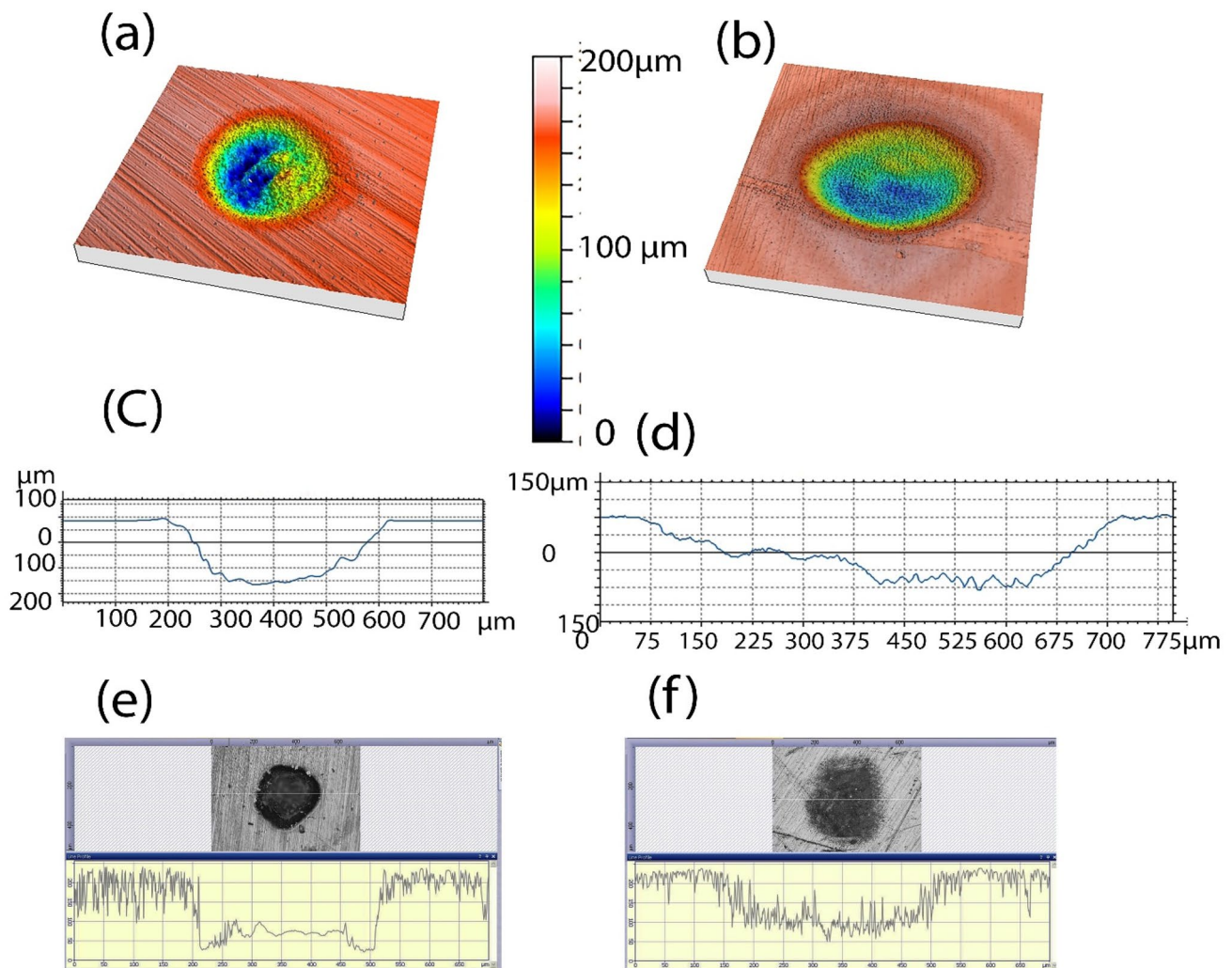


Fig. 8 The confocal and optical microscopic images of ablated crater along with corresponding section profiles formed on the surface of Zn exposed to 1000 laser pulses at a fluence of 2.5 J cm^{-2} with pulse duration of 30 fs. **a, b** Represent confocal microscopic images of Zn

after ablation in air and ethanol, respectively, whereas, **c, d** are corresponding section profiles of **a** and **b**, respectively. The optical microscopic image with section profiles of laser-ablated Zn in air and ethanol are presented in **e, f**, respectively

ablation threshold values for Zn by employing ablation rate method come out to be $F_{\text{th, Zn, Ethanol}} = 1.0 \text{ J cm}^{-2}$ and $F_{\text{th, Zn air}} = 0.4 \text{ J cm}^{-2}$ suggesting that ablation threshold of Zn in air is about two times smaller than ethanol. It employs that micromachining or drilling of materials in more preferable in dry environment than liquid (Fig. 9).

A considerably smaller ablation depth of Zn in ethanol than air is also attributable to the rapid adiabatic cooling and fast heat dissipation of ablated region of the Zn in the presence of ethanol [59, 60]. However, with increasing the fluence, the ablation depth shows an increasing trend for both environments. It is attributable to increased energy deposition with increasing fluence.

3.5 Ablation threshold by ablated volume

The threshold fluence, above which material removal occurs, is also evaluated based on the measured ablated volume from the scanning electron microscopy, confocal microscopy and optical microscopy measurements of laser ablated Zn.

The spatial fluence profile $F [\text{J cm}^{-2}]$ of a laser beam with a Gaussian fluence distribution in polar coordinates (r, z, φ) is expressed as [23],

$$F(r, z, \varphi) = F \exp\left(-\frac{2r^2}{\omega_0^2}\right) \exp\left(-\frac{z}{l}\right) \quad (19)$$

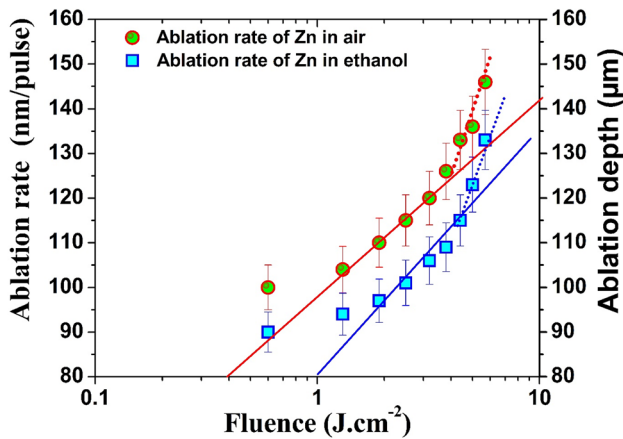


Fig. 9 The variation in the ablation rate and ablation depth of Zn with the increase in the laser fluence for both the environments of air and ethanol after exposure to 1000 applied laser pulses

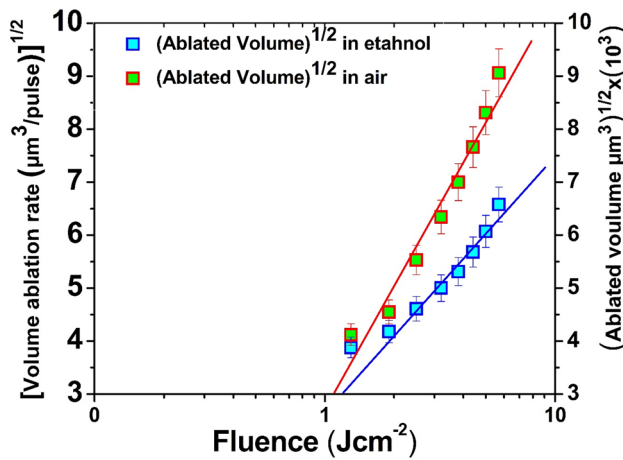


Fig. 10 The variation in volume ablation rate and ablated volume of Zn as function of laser fluence for both the environments of air and ethanol after exposure to 1000 applied laser pulses

where F is the peak fluence, ω_0 is the beam spot radius, l^V is effective penetration depth.

The ablated volume per pulse for the laser beam with Gaussian intensity distribution [23],

$$\Delta V = \frac{1}{4} \pi \omega_0^2 \times l^V \times \left[\ln \left(\frac{F}{F_{th}^V} \right) \right]^2 \tag{20}$$

where l^V and F_{th}^V are fit parameters representing energy penetration depth and threshold fluence, respectively. Figure 10 exhibits the square root of volume ablation rate of Zn as well as square root of ablated volume per 1000 pulses. Each data point in this Fig. is an average of 5 to 10 craters. The threshold fluence comes out to be $F_{th, Zn, Ethanol} = 1.25 \text{ J cm}^{-2}$

and $F_{th, Zn, air} = 1.1 \text{ J cm}^{-2}$ by employing volume ablation rate. The ablation threshold fluence has been evaluated using three methods. All these methods are based on the derivation of ablation threshold using following Eqs. (14–19). As a matter of fact some advantages and disadvantages are associated with each method. For example, the diameter of a crater can be relatively easily determined from a standard/common optical microscopy, (or sometimes by Scanning Electron Microscopy (SEM) as well). Whereas, a relatively expensive 3D profilometer or confocal microscopy is required for determining the depth and volume. Out of the three methods, the diameter method is the most popular, fastest and least expensive method, whereas the ablation rate method is the second popular and moderately expensive method. The least common and scarcely reported method is the volume method in which the complete 3D effects of energy input and resulting crater geometry are considered. In case of irregular crater morphology due to various phenomena such as melting, nonlinear effects, filamentation, self-phase modulation and especially for liquid-assisted ablation of Zn, it is more logical to accept the values obtained using the volume method in this research work. In relation with other reported threshold values, the threshold values reported in this work are in the same order.

The ablation threshold of Zn in ethanol is smaller than in air (by D^2 method). This is associated with an enhancement of the thermal energy coupling during laser ablation, which is more dominant in a denser liquid medium than in air [33]. The other possible important factor responsible for the smaller value of the ablation threshold in ethanol is the confinement effect that enhances collisions between the ablated species and the liquid molecules[61]. In a reactive gas, the high temperature and pressure in the plume result in the formation of gas molecule radicals. The reactions between ablated products and these radicals promote condensation and induce a faster structure growth, which in turn reduces the ablation threshold.

The ablation threshold values of Zn in ethanol are higher than in air with ablation rate method. Whereas, the volume ablation threshold values of Zn in ethanol and air are almost comparable but in ethanol this is slightly higher. This is related to higher ablation depths of Zn in air than ethanol. The adiabatic cooling, incident radiation loss due to scattering from chunk/nanoparticles emitted from the target surface and the dissociation of ethanol molecules hinder the laser energy reaching to the target surface which reduces the removed materials and ablation depth of Zn in ethanol than in air.

A comprehensive comparison of evaluated values of fs laser ablation threshold of Zn with three experimental methods, i.e., (a) D^2 method (diameter of ablated craters), (b) ablation rate variation with fluence in terms of ablated depth and (c) ablation rate variation with fluence in terms of

ablated volume, with analytically evaluated threshold values of Zn evaluated by different methods under different experimental condition reported in the literature [9, 24, 25, 44–48] is presented in Table 2. Our evaluated values of ablation threshold fluence of Zn are comparable with reported values by other groups [21].

The comparison of threshold values of Zn evaluated experimentally in the present study with other reported values are presented in Table 2 and reveal:

The ablation threshold values of Zn in ethanol have not been reported by any research group, therefore these values cannot be compared. However, our ablation threshold values of Zn in air varies from 0.4 to 1.1 J cm⁻². These values are significantly greater than analytically evaluated values of threshold ablation fluence $F_{th} = \frac{\rho\Omega_{vap}}{\alpha A} \text{ J cm}^{-2} = 0.27 \text{ J cm}^{-2}$, by Nielsen et al. [53] and $F_{th} = \frac{3}{8}(\epsilon_b + \epsilon_{esc})\frac{\lambda n_c}{2\pi} \text{ J cm}^{-2} = 0.21 \text{ J cm}^{-2}$, by Gamaly et al. [50]. This higher values of experimentally evaluated ablation threshold is attributed to scattering, reflection and absorption of incoming laser radiations by shockwaves and in air environment.

Our values are comparable with threshold values evaluated by ultrafast pump-probe imaging method [67], which are 1.1–1.8 J cm⁻² for solid density plasma and 0.34 J cm⁻² for phase explosion with 65 fs pulse duration. The values obtained by ablation rate method varies from 1.5 to 0.35 J cm⁻² [64] for 70 fs and are also comparable with our values. However, the values obtained by D^2 method by same group are smaller than our values, because of different ablation fluence regimes. The research groups who have used laser beams with larger pulse duration of ns or ps, their evaluated ablation threshold values cannot be compared our evaluated values.

3.6 Compositional analysis

3.6.1 ATR analysis

ATR analysis of laser-irradiated Zn in air and ethanol in range of wavenumbers of 500–900 cm⁻¹ is presented in Fig. 11a. The peak is identified at wavenumber of 513 cm⁻¹ and corresponds to ZnO [68]. Zn reaction with the present oxygen in ethanol and air is responsible for the formation of ZnO [69]. ATR analysis of laser ablated Zn for the wavenumber range of 2250–2450 cm⁻¹ is shown in Fig. 11b. Two peaks are identified at wave numbers of 2341 cm⁻¹ and 2359 cm⁻¹. The appearance of these two peaks also represents the presence of ZnO on the Zn surface [70] after ablation in air and ethanol. It is observed that the peak intensity of ZnO (metal oxide) is more sharp and intense in ethanol as compared to air. This is attributable to enhanced confinement effect of plasma in liquid than in air. High pressure in front of expanding plume provides better way for reaction of ablated species with that dissolved in the liquid media

such as oxygen [71]. ATR analysis for the frequency range of 1300–1700 cm⁻¹ for exposed Zn in ethanol (alcohol) is displayed in Fig. 11c. Two strong peaks are identified at wavenumbers of 1380 and 1640 cm⁻¹. These bands correspond to C=O stretching vibration and C–H stretching vibration, respectively [68]. These bands are associated with the presence of enol type of complex (metal–acetylacetonate compound) after the reaction of alcohol with Zn. The laser ablation of Zn in the presence of ethanol causes to react metallic ions and alcohol molecules. Consequently, the cluster formation takes place which forms metal–ethanol complex clusters (Zn⁺ (CH₃OH)_n and protonated ethanol clusters H⁺ (CH₃OH)_n [72].

3.6.2 XRD analysis

XRD analysis of laser-ablated Zn in air and ethanol is shown in Fig. 12. The peak is identified at 2θ of 34° and corresponds to the crystalline structure with (002) preferred orientation. It also confirms the formation of ZnO after ablation of Zn in both environments. The enhanced peak intensity of (002) plane after ablation of Zn in ethanol than in air again confirms that liquid-assisted ablation is more favourable for enhanced chemical reactivity.

3.7 Hardness analysis

Figure 13 shows the variation in hardness of femtosecond laser-irradiated Zn targets as a function of laser fluence in air and ethanol. The hardness value for the untreated Zn sample is 28 HV. For both environments, it is observed that hardness of treated samples increases significantly with increasing fluences. However, in case of treatment in ethanol, higher values of hardness of Zn are observed than in air.

The increase in hardness of treated Zn in case of both environments is attributable to interstitial diffusion of oxygen into the lattice resulting into decrease in crystallite size and tensile residual stresses [46] as well as formation of ZnO [50]. Smaller crystallite size is efficient in obstructing the dislocation movement and is responsible for high strength and hardness. Laser thermal strengthening of Zn, during and after the irradiation stage is due its transformation into decomposition products on sudden cooling. In addition, phase and structural transformations occur under conditions far from equilibrium as a result of extremely high heating and cooling rates during the laser ablation process.

The higher value of hardness of the irradiated Zn in ethanol as compared to air environment can be explained on the basis of enhanced diffusion of Oxygen across the grain boundaries at extreme pressure and temperature conditions of liquid-confined environment. It results in enhanced chemical reactivity of Zn with ethanol and formation of oxides

Table 2 A comparison of evaluated values of laser ablation threshold of Zn with reported values in the literature [9, 24, 25, 44–48]

Pulse duration	Wavelength [nm]	Fluence threshold [J cm^{-2}]	Method	Defined as/for	References
30 fs		(a) $F_{\text{th, Zn, Ethanol}} = 0.53 \text{ J cm}^{-2}$ $F_{\text{th, Zn, air}} = 1.0 \text{ J cm}^{-2}$ (b) $F_{\text{th, Zn, Ethanol}} = 1.0 \text{ J cm}^{-2}$ $F_{\text{th, Zn, air}} = 0.4 \text{ J cm}^{-2}$ (c) $F_{\text{th, Zn, Ethanol}} = 1.25 \text{ J cm}^{-2}$ $F_{\text{th, Zn, air}} = 1.1 \text{ J cm}^{-2}$	Three methods (a) D^2 method (diameter of ablated craters) (b) Ablation rate variation with fluence in terms of ablated depth (c) Ablation rate variation with fluence in terms of ablated volume	Ablation threshold	Present Experimental study
30 fs	800	0.27 J cm^{-2}	Threshold ablation fluence $F_{\text{th}} = \frac{\rho \lambda^2 \nu_{\text{vap}}}{\alpha A} \text{ J cm}^{-2}$, Nielsen et al. [53]	Ablation threshold	Present analytical study
30 fs	800	0.21 J cm^{-2}	The threshold laser fluence for ablation of metals $F_{\text{th}} = \frac{3}{8} (\epsilon_b + \epsilon_{\text{esc}}) \frac{\lambda n_c}{2\pi} \text{ J cm}^{-2}$, Gamaly et al. [50]	Ablation threshold	Present analytical study
6.7 ps	515	0.1 J cm^{-2} and 0.68 J cm^{-2}	Ablation rate with the variation of fluence in terms of ablated volume	Ablation threshold	[22]
6.7 ps	1030	(a) 0.39 J cm^{-2} (b) 0.33 J cm^{-2} (c) 0.21 J cm^{-2}	Three methods (a) D^2 method (b) Ablation rate per unit of fluence in terms of ablated depth in terms of ablated volume (c) Ablation rate per unit of fluence	Ablation threshold	[23]
6.7 ps	1030 And 515	0.4 J cm^{-2} , 0.14 J cm^{-2} For smooth surfaces 0.4 for both wavelengths after improved surface roughness and surface area	D^2 method	Ablation threshold for rough surfaces	[21]
5 ns	1064 532 266	1.42 J cm^{-2} 0.91 J cm^{-2} 3.12 J cm^{-2}	Laser-induced breakdown spectroscopy	Plasma threshold	[62]
~ 1 ps	780	0.5 J cm^{-2}	Optically detectable damage	Melting threshold	[63]
70 fs	800	1.5 J cm^{-2} 0.35 J cm^{-2} 0.35 J cm^{-2} 0.2 J cm^{-2} 0.03 J cm^{-2}	Ablation rate D^2 method	$N \leq 128$ $N > 128$ $4 \leq F \leq 14 \text{ J cm}^{-2}$ $0.1 \leq F \leq 4 \text{ J cm}^{-2}$ $0.018 \leq F \leq 0.01 \text{ J cm}^{-2}$	[64]
65 fs	800	0.052 J cm^{-2}	Optically detectable damage	Ablation threshold	[65]
200 fs	800	0.102 J cm^{-2}	Optically detectable damage	Laser-Induced Forward Transfer	[66]

Table 2 (continued)

Pulse duration	Wavelength [nm]	Fluence threshold [J cm^{-2}]	Method	Defined as/for	References
65 fs	800	0.022 J cm^{-2}	Optically detectable damage	Damage threshold	[67]
		0.1 J cm^{-2}	Ultrafast pump-probe imaging	spallation	
		0.34 J cm^{-2}		Phase explosion	
		1.1–1.8 J cm^{-2}		Solid density plasma	

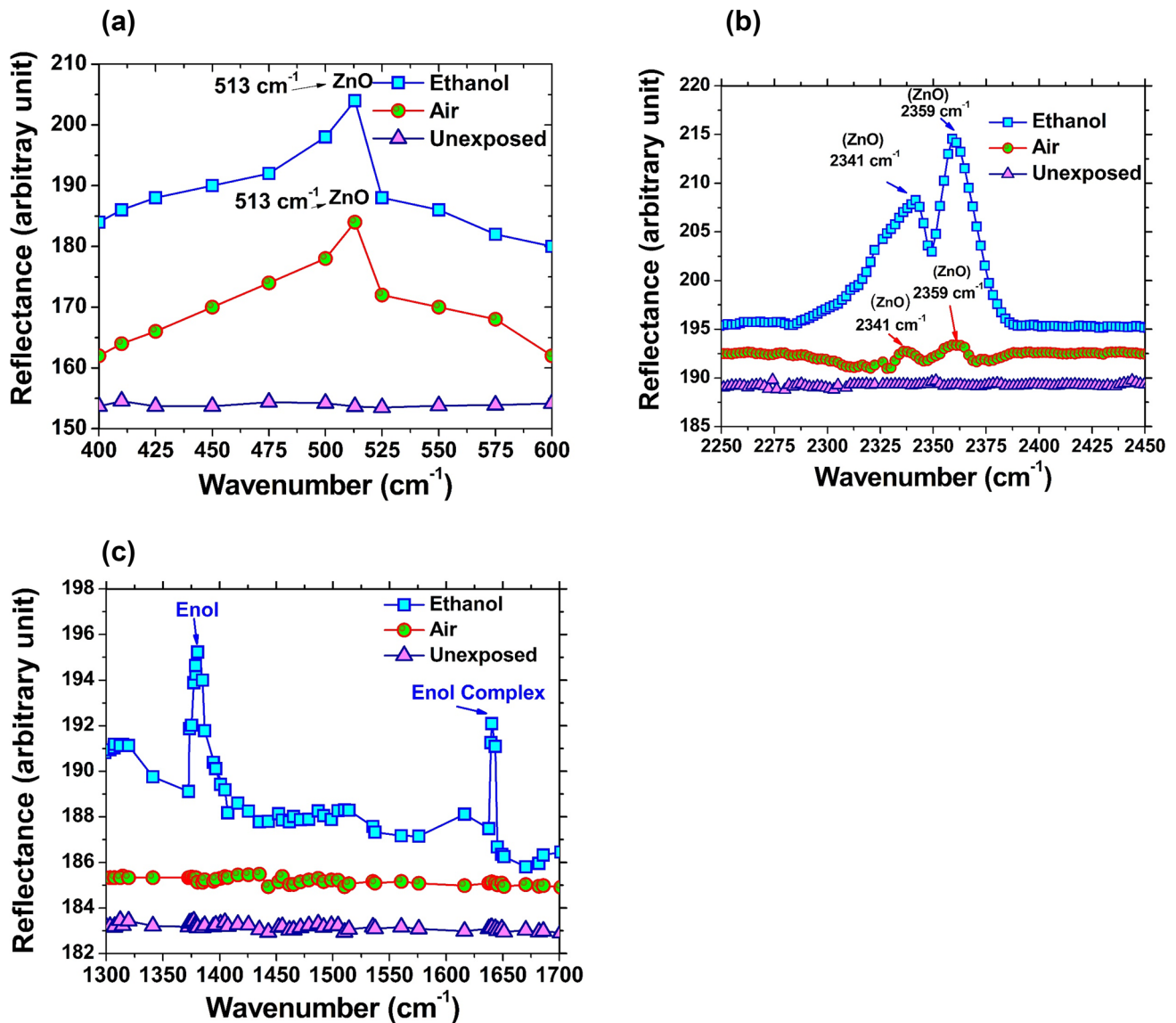


Fig. 11 ATR-FTIR spectra of unexposed and fs laser-ablated Zn for a pulse duration of 30 fs, **a** ATR-FTIR spectral range 400–600 cm^{-1} , exhibiting the formation of zinc oxides at 513 cm^{-1} in both environments of air and ethanol, **b** ATR-FTIR spectral range of 2250–2450 cm^{-1} , for both environments of air and ethanol exhibiting the formation of zinc oxides at wavenumbers of 2341 cm^{-1} and

2359 cm^{-1} , **c** ATR-FTIR spectral range of 1300–1700 cm^{-1} , for only ethanol exhibiting two strong peaks at wavenumbers of 1380 cm^{-1} and 1640 cm^{-1} representing the formation of enol and enol complex after exposure to 1000 laser pulses at a fluence of 2.5 J cm^{-2} . In unexposed Zn target and after its exposure in air no enol and enol complex are formed

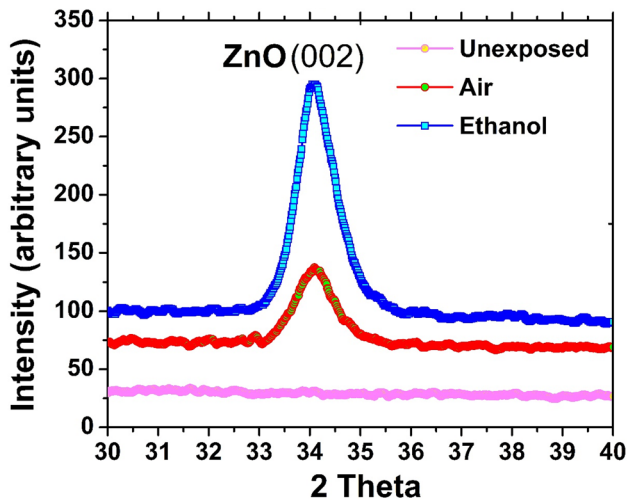


Fig. 12 XRD analysis of unexposed and fs laser-ablated Zn in both air and ethanol environments at the pulse duration of 30 fs representing the formation of ZnO phase with crystalline structure of (002) preferred orientation after exposure to 1000 laser pulses at a fluence of 2.5 J cm^{-2}

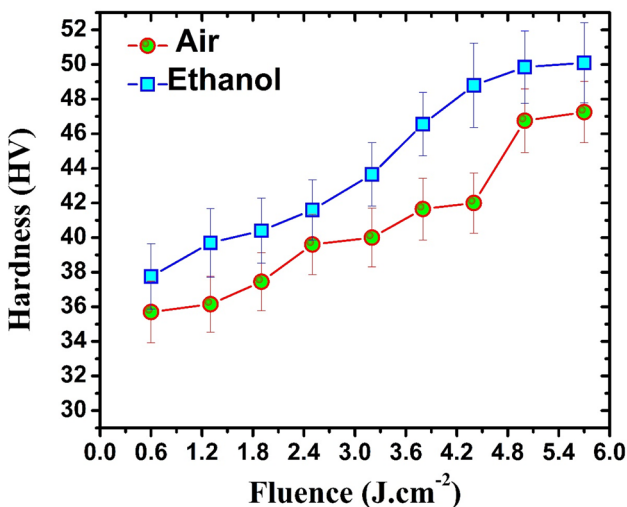


Fig. 13 The variation in hardness of femtosecond laser irradiated Zn targets as a function of laser fluence in ambient environment of air and ethanol after exposure to 1000 laser pulses of pulse duration 30 fs

(confirmed by both XRD and FTIR analyses) which are responsible for increased value of hardness [50].

The laser-induced shock pressure [73] and mechanical/ablation pressure [31] during ablation of materials by intense laser pulse is one of possible cause for surface hardening. Ultrafast lasers provide very different conditions for the shock-induced hardening. The magnitude of surface hardening depends on the laser shocking conditions and nature of the target material. One of the important parameters is the peak pressure. The peak pressure induced by the Laser

Shock Processing (LSP) is directly proportional to laser intensity, therefore for shorter pulse duration, laser intensity is higher and laser-induced shock processing pressure also increases which is considered to be responsible for enhancement of microhardness of laser-irradiated Zn [74]. The laser-induced shock pressure is expressed as follows [73]

$$P(\text{Mbar}) = 11.6 \left(\frac{I}{10^{14}} \right)^{3/4} \lambda^{-1/4} \left(\frac{A}{2Z} \right)^{7/16} \left(\frac{Z \times \tau}{3.5} \right)^{-1/8} \quad (21)$$

where I is the irradiance on target with the unit of W cm^{-2} , λ is the laser wavelength in μm , A and Z are, respectively, the mass number (65.39) and the atomic number (30) of the Zn target and τ is the pulse duration of laser beam in ns. The pressure of the shock-waves is directly proportional to the (laser pulse peak intensity)^{3/4}.

Similarly the ablation pressure (P_a) is expressed as below [31]

$$P_a(\text{bar}) = b \times I^{0.7} \left(\text{MW/cm}^2 \right) \times \lambda^{0.3} (\mu\text{m}) \times \tau^{-0.15} (\text{ns}) \quad (22)$$

where b is the material dependent coefficient ranging from 3.9 to 6.5 [31].

The variation in laser-induced shock pressure (GPa) and laser ablation pressure (GPa) of 30 fs laser-irradiated Zn targets as a function of laser fluence is shown in Fig. 14. Both show an increasing trend with increasing laser fluence. However, in ethanol, the confinement process increases the life time of shock waves [31] and the target acquires higher impulse momentum due to the induced shock wave. The growth of various structures on Zn surface is strongly influenced directly by the laser fluence and the combined surface treatment. The generation of residual compressive stresses after laser irradiation also enhances the material hardness [75].

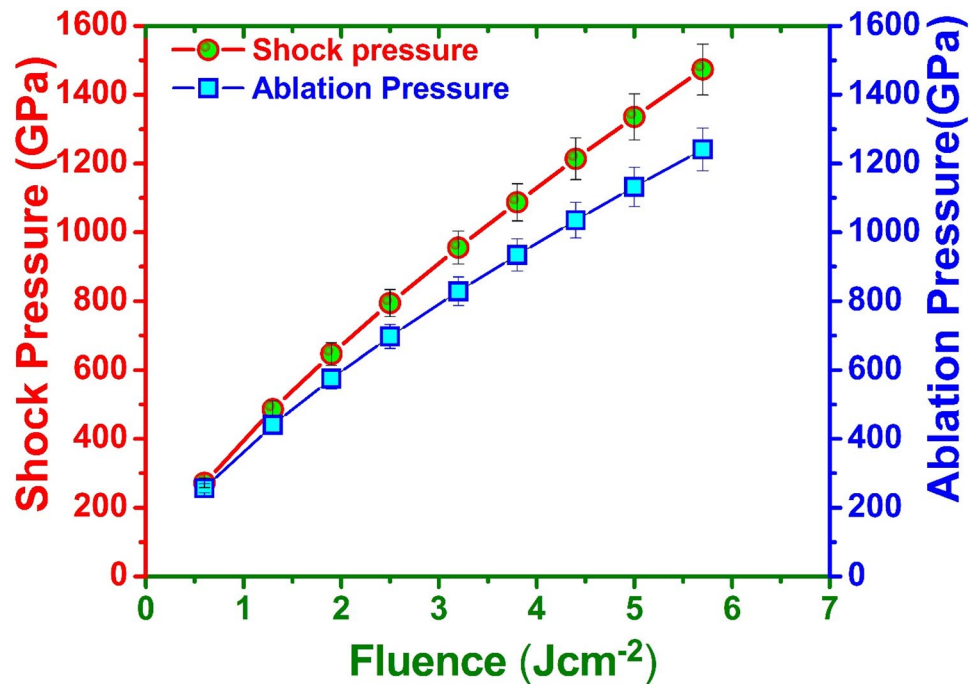
4 Conclusions

The effect of increasing irradiation fluence of femtosecond laser on surface morphology, ablated area, ablation depth, ablated volume, structural modification and hardness of Zn in ambient environment of air and ethanol has been investigated.

At lower fluence, in air, nanostructures are more distinct and well defined and they become merged, fused and indistinguishable at high fluences. In ethanol, with increasing fluence, the dot-like structures are transformed into porous and bowl-shaped structures.

For all the fluences, ethanol environment plays an important role for the growth of small scale surface structures. The presence of liquids offers cleaner surface

Fig. 14 The variation in laser-induced shock pressure (GPa) and laser ablation pressure (GPa) of 30 femtosecond laser irradiated Zn targets as a function of laser fluence



ablation than air. In case of air, at the center as well as at the periphery, there is a non-uniform surface morphology with an appearance of both micro and nanoscale droplets, particulates and rims. In ethanol environment, nanoscale colloids, droplets, pores and bowl-shaped cavities are formed. Ablation of Zn in ethanol is favorable to ablate larger areas. Whereas, the ablation in air is more suitable for the formation of deeper craters.

The ablation threshold fluence of Zn for 800 nm wavelength and 30 fs pulse duration is evaluated analytically as well as experimentally by employing three methods, i.e., squared diameter, depth ablation rate, and volume ablation rate. The evaluated value of ablation threshold fluence of Zn by squared diameter, and volume ablation rate is smaller in ethanol than air. Whereas, the value of ablation threshold fluence of Zn using a method of ablation depth and ablation volume is higher in case of air than ethanol.

For both environments, the hardness of treated samples increases significantly with the increase in the fluence. However the irradiation of Zn in ethanol is more favourable for the increase in the hardness of Zn as compared to that in air.

Acknowledgements The first author is thankful to OeAD (Austrian Agency for International Cooperation in Education and Research) Austria for funding Ernst Mach Follow-up Grant for funding 3 months post doctorate to stay at Austria

Compliance with ethical standards

Conflicts of interest The authors declare no conflicts of interest.

References

1. M. Akram, S. Bashir, S.A. Jalil, M. Elkabbash, F. Aumayr, A. Ajami, W. Husinsky, K. Mahmood, M.S. Rafique, C. Guo, *Opt. Mat. Exp.* **9**, 3183 (2019)
2. L. Jiang, H.L. Tsai, *Appl. Phys. Lett.* **87**, 151104 (2005)
3. D.S. Ivanov, B. Rethfeld, *Appl. Surf. Sci.* **255**, 9724 (2009)
4. S. Bashir, M.S. Rafique, C.S. Nathala, W. Husinsky, *Appl. Surf. Sci.* **90**, 53 (2014)
5. N.M. Bulgakova, V.P. Zhukov, A.Y. Vorobyev, C. Guo, *Appl. Phys. A* **92**, 883 (2008)
6. S. Bashir, M.S. Rafique, W. Husinsky, *Appl. Surf. Sci.* **255**, 8372 (2009)
7. S. Bashir, M.S. Rafique, W. Husinsky, *Rad. Eff. Def. Solids* **168**, 902 (2013)
8. F. Costache, S. Eckert, J. Reif, *Appl. Surf. Sci.* **252**, 4416 (2006)
9. R. Fang, A. Vorobyev, C. Guo, *Light Sci. Appl.* **6**, e16256 (2017)
10. J. Zhang, Y. He, B. Lam, C. Guo, *Opt. Exp.* **25**, 20323 (2017)
11. P. Lorazo, L.J. Lewis, M. Meunier, *Phys. Rev. B* **73**, 134108 (2006)
12. N. Maharjan, W. Zhou, Y. Zhou, Y. Guan, N. Wu, *Surf. Coat. Tech.* **366**, 311 (2019)
13. S. Bashir, M.S. Rafique, W. Husinsky, *Nucl. Inst. Meth B* **349**, 230 (2015)
14. E.B. Barmina, E. Stratakis, C. Fotakis, G.A. Shafeev, *Quant. Elect.* **40**, 1012 (2010)
15. N. Lasemi, U. Pacher, L.V. Zhigilei, O. Bomati-Miguel, R. Lahoz, W. Kautek, *Appl. Surf. Sci.* **433**, 772 (2018)
16. A.S. Nikolov, I.I. Balchev, N.N. Nedyalkov, I.K. Kostadinov, D.B. Karashanova, G.B. Atanasova, *Appl. Phys. A* **2017**, 123 (2017)
17. J. Yong, Z. Zhan, S.C. Singh, F. Chen, C. Guo, *Langmuir* **35**, 9318 (2019)
18. E.V. Barmina, M. Barberoglu, V. Zorba, A.V. Simakin, E. Stratakis, C. Fotakis, G.A. Shafeev, *Quant. Elect.* **39**, 89 (2009)
19. S. Bashir, M. Shahid-Rafique, A. Ajami, W. Husinsky, I.K. Umm, *Appl. Phys. A* **113**, 673 (2013)

20. E.V. Barmina, A.A. Serkov, E. Stratakis, C. Fotakis, V.N. Stolyarov, I.N. Stolyarov, G.A. Shafeev, Appl. Phys. A **106**, 1 (2012)
21. H. Mustafa, M. Mezera, D.T.A. Matthews, G.R.B.E. Römer, Appl. Surf. Sci. **488**, 10 (2019)
22. H. Mustafa, D.T.A. Matthews, G.R.B.E. Römer, Mat. Des. **169**, 107675 (2019)
23. H. Mustafa, R. Pohl, T.C. Bor, B. Pathiraj, D.T.A. Matthews, G.R.B.E. Römer, Opt. Exp. **26**, 18664 (2018)
24. H. Mustafa, M. Jalaal, W. Ya, N. Ur-Rahman, D.T.A. Matthews, G.R.B.E. Römer, J. Laser Micro Nanoeng. **13**, 178 (2018)
25. B.N. Chichkov, C. Momma, S. Nolte, F. von Alvensleben, A. Tünnermann, Appl. Phys. A **63**, 109 (1997)
26. S. Nolte, C. Momma, H. Jacobs, A. Tünnermann, B.N. Chichkov, B. Welleghausen, H. Welling, JOSA B **14**, 2716 (1997)
27. J.M. Liu, Opt. Lett. **7**, 196 (1982)
28. A. Garcia-Giron, D. Sola, J.I. Peña, Appl. Surf. Sci. **363**, 548 (2016)
29. H. Liu, F. Chen, X. Wang, Q. Yang, H. Bian, J. Si, X. Hou, Thin Solid Films **518**, 5188 (2010)
30. L. Berthe, R. Fabbro, P. Peyre, E. Bartnicki, J. Appl. Phys. **85**, 7552 (1999)
31. R. Fabbro, J. Fournier, P. Ballard, D. Devaux, J. Virmont, J. Appl. Phys. **68**, 775 (1990)
32. T.J.Y. Derrien, R. Koter, J. Krüger, S. Höhm, A. Rosenfeld, J. Bonse, J. Appl. Phys. **116**, 074902 (2014)
33. A.Y. Vorobyev, C. Guo, J. Phys. Conf. Ser. **59**, 579 (2007)
34. D. Zhang, C. Zhang, J. Liu, Q. Chen, X. Zhu, C. Liang, ACS Appl. Nano Mater. **2**, 28 (2019)
35. D. Zhang, B. Gökce, S. Barcikowski, Chem. Rev. **117**, 3990 (2017)
36. S.C. Singh, R.K. Kotnala, R. Gopal, J. Appl. Phys. **118**, 064305 (2015)
37. T. Sasaki, Y. Shimizu, N. Koshizaki, J. Photochem Photobiol. A: Chem. **182**, 335 (2006)
38. J. Bonse, J. Krüger, J. Appl. Phys. **108**, 034903 (2010)
39. J.E. Sipe, A. Young, F. Jeff, J. S. Preston, H. M. van-Driel, Phys. Rev. B **27**:141 (1983)
40. K. Okamuro, M. Hashida, Y. Miyasaka, Y. Ikuta, S. Tokita, S. Sakabe, Phys. Rev. B **82**, 165417 (2010)
41. S. Sakabe, M. Hashida, S. Tokita, S. Namba, K. Okamuro, Phys. Rev. B **79**(3), 033409 (2009)
42. M.H. Hong, K.Y. Ng, Q. Xie, L.P. Shi, T.C. Chong, Appl. Phys. A **93**, 153 (2008)
43. P. Lorazo, L.J. Lewis, M. Meunier, Phys. Rev. B **73**, 1 (2006)
44. Y. Shimotsuma, P.G. Kazansky, J. Qiu, K. Hirao, Phys. Rev. Lett. **91**, 247405 (2003)
45. G. Miyaji, K. Miyazaki, Opt. Exp. **16**, 16265 (2008)
46. G.W. Yang, Prog. Mat. Sci. **52**, 648 (2007)
47. C. Li, J. Wang, X. Wang, Phys. Lett. A **378**, 3319 (2014)
48. M. Chen, L. Xiangdong, Y. Liu, M. Zhao, Chin. Opt. Lett. **10**, 051402 (2012)
49. J. Bonse, S. Höhm, S.V. Kirner, A. Rosenfeld, J. Krüger, IEEE J. Quant. Elect. **23**, 1 (2017)
50. E.G. Gamaly, A.V. Rode, B. Luther-Davies, V.T. Tikhonchuk, Phys. Plasmas **9**, 949 (2002)
51. D.R. Paschotta, The Encyclopedia of Laser Physics and Technology, <http://www.rp-photonics.com/encyclopedia.html> (2019)
52. M.Z. Butt, Laser ablation characteristics of metallic materials: Role of Debye-Waller thermal parameter. IOP Conf. Ser. Mat. Sci. Eng. **60**, 012068 (2014)
53. J. Byskov-Nielsen, J.M. Savolainen, M.S. Christensen, P. Balling, Appl. Phys. A **101**, 97 (2010)
54. F.C. Porter, Zinc Handbook: Properties, Processing, and Use in Design. CRC Press. [http://refhub.elsevier.com/S0169-4332\(19\)31373-X/rf0095](http://refhub.elsevier.com/S0169-4332(19)31373-X/rf0095) (1991)
55. M. Hashida, A.F. Semerok, O. Gobert, G. Petite, Y. Izawa, J.F. Wagner, Appl. Surf. Sci. **197–198**, 862 (2002)
56. J. Jandeleit, G. Urbasch, H.D. Hoffmann, H.G. Treusch, E.W. Kreutz, Appl. Phys. A **63**, 117 (1996)
57. M. Akram, S. Bashir, A. Hayatat, K. Mahmooda, R. Ahmad, M.K. Rahaman, Laser Part. Beams **32**, 119 (2014)
58. A.Y. Vorobyev, C. Guo, J. Nano Res. **14**, 57 (2011)
59. L.M.J. Santillán, F.A. Videla, M.B. Fernández van Raap, D.C. Schinca, L.B. Scaffardi, J. Appl. Phys. **113**, 134305 (2013)
60. L. Berthe, R. Fabbro, P. Peyre, L. Tollier, E. Bartnicki, J. Appl. Phys. **82**(6), 2826–2832 (1997)
61. A. Pereira, A. Cros, P. Delaporte, S. Georgiou, A. Manousaki, W. Marine, M. Sentis, Appl. Phys. A **79**, 1433 (2004)
62. L.M. Cabalin, J.J. Laserna, Spectrochim. Acta B: Atomic Spect. **53**, 723 (1998)
63. M.B. Agranat, S.I. Ashitkov, V.E. Fortov, A.V. Kirillin, A.V. Kostanovskii, S.I. Anisimov, P.S. Kondratenko, Appl. Phys. A **69**, 637 (1999)
64. A.F.S. M. Hashida, O. Gobert, G. Petite, J. F. Wagner, Nonresonant Laser-Matter Interaction (NLMI-10), (International Society for Optics and Photonics) (2001), p. 178
65. A.Y. Vorobyev, C. Guo, Opt. Exp. **14**, 13113 (2006)
66. A. Klini, P.A. Loukakos, D. Gray, A. Manousaki, C. Fotakis, Opt. Exp. **16**, 11300 (2008)
67. R. Fang, A. Vorobyev, C. Guo, Light Sci. Appl. **6**, 1 (2017)
68. S. George, *Infrared and Raman Characteristic Group Frequencies (Tables and Charts) (Third Edition)* (Wiley, England, 2001).
69. K. Sasaki, T. Nakano, W. Soliman, N. Takada, Appl. Phys. Exp. **2**, 0465011 (2009)
70. W.M. Hlaing, Infrared spectroscopy of zinc oxide and magnesium nanostructures, in: Materials Science Program, Washington State University (2007)
71. H.W. Kang, H. Lee, A.J. Welch, J. Appl. Phys. **103**, 083101 (2008)
72. N.D. Mei, L.H. Yang, S.D. Zhang, Chin. J. Chem. **24**, 750 (2006)
73. H.I. Wang, W.T. Tang, L.W. Liao, P.S. Tseng, C.W. Luo, C.S. Yang, T. Kobayashi, J. Nanomaterials **1**, 1 (2012)
74. M.A.M.A.L.E. Murr, *Shock Waves and High-Strain-Rate Phenomena In Metals* (Plenum Publishing Corporation, New York, 1981).
75. J.S. Hoppius, L.M. Kukreja, M. Knyazeva, F. Pöhl, F. Walther, A. Ostendorf, E.L. Gurevich, Appl. Surf. Sci. **435**, 1120 (2018)

Publisher's Note Springer Nature remains neutral with regard to jurisdictional claims in published maps and institutional affiliations.